Faculdade de Engenharia da Universidade do Porto

FEUP

Elasto-plastic analysis of structures using an Isogeometric Formulation

João Pedro Ferreira

Mestrado Integrado em Engenharia Mecânica

Supervisor: Marco P.L. Parente (Post-PhD Researcher and Auxiliar Professor)

Second Supervisor: Renato M. Natal Jorge (Associated Professor)

July 18, 2014

Elasto-plastic analysis of structures using an Isogeometric Formulation

João Pedro Ferreira

Mestrado Integrado em Engenharia Mecânica

July 18, 2014

Abstract

Numerical simulation often involves using the Finite Element Method (FEM) where the geometry model, derived from CAD systems, usually suffer a reparameterization of the CAD geometry by piecewise low order polynomials. This information transfer between models suitable for design (CAD) and analysis (FEM) introduces significant approximation errors and entails a amount of man-hours to generate a suitable finite element mesh.

In order to create industrial metal parts suitable for the imposed tasks, in which meet the geometrical and mechanical requirements combined with reduced manufacturing costs, requires a continuous evolution of assistive technology in order to innovate and optimise the different stages of the production processes.

In this work it is intended to contribute to the analysis of forming processes and pipeline applications by discussing the use of an isogeometric approach into a finite element pre-developed models.

Thus, this dissertation makes a study of how ductile materials behave when subjected to monotonic and cyclic mechanical loads. Isogeometric models with a small and large strains formulations, plasticity with isotropic hardening and plasticity with kinematic hardening are developed. Also, an introduction to a Lemaitre-based damage model is designed. The Bauschinger effect, the mesh dependence ,and the differences between the developed small and finite strain models are evaluated by comparison with the finite element typical discretization models.

The isogeometric discretization was performed taking the advantages of the symbolic and algebraic interfaces of the AceGen software. Previous developed elasto-plastic finite element models were included into an hyperelastic isogeometric model using the AceGen and AceFEM systems.

Resumo

Na maior parte das vezes, as simulações numéricas que envolvem o uso do Método dos Elementos Finitos, onde a geometria dos modelos criados, derivada dos sistemas CAD, normalmente sofre uma reparameterização através de polinómios de baixo grau. Esta transferência de informação entre os dois sistemas introduz erros de aproximação e custa muitas horas de trabalho para gerar uma malha que possa ser analisada.

De forma a criar peças industriais que cumprem as tarefas propostas, com o controlo das suas dimensões e propriedades mecânicas, combinado com baixos custos de produção, requer uma evolução continua na tecnologia de assistência à inovação e otimização em todas as fases da produção.

Neste trabalho pretende-se contribuir para a análise nos processos de conformação discutindo o uso de uma formulação isogeométrica a partir de modelos em elementos finitos já desenvolvidos.

Por conseguinte, esta dissertação estuda o comportamento de materiais ductéis quando sujeitos a cargas monotónicas e cíclicas. São desenvolvidos modelos isogeométricos com plasticidade através de formulações para baixos e grandes deslocamentos, com encutruamento isotrópico e cinemático . Também se introduz o modelo de dano de Lemaitre. Os resultados são comparados com os modelos em elementos finitos através do estudo da influência da malha,do efeito de Bauschinger e da diferença entre uma formulação para baixos deslocamentos e outra para grandes deslocamentos.

A discretizações isogeométricas foram realizadas usufruindo das vantajens de cálculo simbólico do software AceGen.

Acknowledgements

Ao meu orientador, Prof. Marco Paulo Lages Parente, pela sua compreensão e apoio em todos os momentos ao longo deste trabalho, pelo seu espírito alegre e cativante. Pelas oportunidades proporcionadas, demonstro a minha mais sincera gratidão.

Também deixo aqui a minha palavra de apreço ao Prof. Renato Manuel Natal Jorge, pela sua personalidade empreendedora e pela sua vasta experiência. Fatores estes que conseguiram dar um rumo ao trabalho desenvolvido. Pela confiança depositada, um enorme obrigado.

Aos meus amigos e colegas de curso. Ao Pedro Sousa, pela sua genialidade e espírito trabalhador. Ao Henrique Duarte, pela sua intuição e sensibilidade nos mais variados problemas. Ao Rafael Tavares, não só pela boa disposição como também pelos inúmeros alertas para trabalhar quando se deve fazê-lo. Ao José Rafael Andrade, pelo seu espírito crítico e pelas imensas discussões frutíferas. Ao Francisco Rua, por levantar questões que mais ninguém se lembraria. Ao Tiago Ramos, Rui Ormonde, Viktor Csaky, Márcio Fernandes, Francisco Torres, e muitos outros. Obrigado por me ajudarem, mais do que imaginam, a concretizar a passo e passo o curso.

Agradeço a ti, Beatriz Couto, que durante estes 5 anos sempre estiveste a meu lado e me apoiaste como ninguém. Surpreendeste-me e me deste-me forças para não desistir. Novamente, obrigado.

À minha família. Pelo apoio incondicional e por me amarem. À minha irmã, que não me deixou desistir do curso. À minha mãe, pelo apoio constante. Ao meu pai, por ser o alicerce inquebrável. E ao resto da família, obrigado.

A ti, meu avô, que sei que consegues ler estas palavras. Jamais terei palavras para agradecer tudo o que fizeste por mim. Com um aperto no coração, dedico-te todo o trabalho.

João Ferreira

"A good scientist is a person with original ideas. A good engineer is a person who makes a design that works with as few original ideas as possible. There are no prima donnas in engineering."

Freeman Dyson

Contents

List of Figures

List of Tables

Abbreviations

CDM	Continuum Damage Mechanics
IBVP	Initial Boundary Value Problem
NLF	Non-Local Formulation
FEM	Finit Element Method
RVE	Representative Volume Element
FEA	Finit Element Analysis
CAD	Computer-Aided Design
NURBS	Non-Uniform Rational B-Spline
IGA	IsoGeometric Analysis
ASG	Analysis Suitable Geometry
PDEs	Partial Differencial Equations system
NURBS	Non-Uniform Rational B-splines

Chapter 1

Introduction

1.1 Context

1.1.1 Ductile steels Dimensioning

In recent years, the numerical modelling of metal forming processes has been instrumental in supporting the industry, providing design and manufacture tools for metallic machines and products. To create industrial metal parts suitable for the imposed tasks, which meet the geometrical and mechanical requirements combined with reduced manufacturing costs, requires a continuous evolution of assistive technology in order to innovate and optimise the different stages of the production processes.

In general, in the plastic forming processes, a metal part is plastically deformed between tools and/or molds to obtain the desired geometry. Therefore, the geometric form of the tool and its movement are important factors to obtain the final (usual complex) geometry. However, in some cases the challenges pass trough the elimination of undesirable effects such as degradation of material properties, surface defects, or even the collapse of the material. In other point of view, the key to obtaining a desired shape is the control of the metal flow, but the properties of the final product are highly influenced by the strain field, the strain rate, temperature, temperature gradient and other physical quantities. Understanding the combination of different thermo-mechanical phenomena during a forming operation is not a trivial task and forms several computational implementation challenges.

Knowing the exact locations where the crack initially occurs during the plastic deformation is of great importance, since this information can indicate the possibility of defects, which leads to a decreasing number of parts rejected.

Experimental techniques to obtain the evolution of stress and strain field history usually are not sophisticated and sometimes may be inaccurate when the load path is more complex, and therefore it will be essential the use mathematical models to simulate the

entire forming process. Their use allows to improve and facilitate the design of parts, thus minimising the use of trial and error procedures, characterised by their expensive costs.

In addition, the concepts developed along this work can also applied on steel members subjected to extreme loading conditions and large deformations, for example in pipeline applications. This kind of structures are associated with widespread yielding, which usually leads to fracture, either due to monotonic loading or ultra-low-cycle fatigue (ULCF).

The initiation and growth of cavities and micro-cracks induced by large deformations in metals is a phenomenon usually described by the gradual internal deterioration, or damage over the load path, which is frequently followed by the occurrence of macroscopic failure in common engineering materials such as steel, aluminium and copper alloys [4]. This type of investigations are of crucial importance for the industrial scenario nowadays [5].

The phenomena of deterioration mechanisms when materials are subjected to loading are evaluated at different scales. At the micro-scale level occurs the accumulation of micro-stresses in the neighbourhood of defects or interfaces and the breaking of bonds. At the mesoscale level of the representative volume the damage is the growth and the coalescence of micro-cracks or micro voids which together initiates the propagation of a crack. At the macro-scale level the growth of that crack takes place [6]. In other words, the micro-scale level is the scale of mechanisms used to consider strains and damage but the constitute equations in order to describe the damage evolution are written at the mesoscale level. After that, the crack propagation is evaluated in a macro-scale level.

Many researches have been made in order to develop material laws that have the ability of reproducing the experiments observations through the establishment of yield functions. After this first developments, the material degradation along time should be taken into account to predict the behaviour accurately in practical engineering problems, for example, in metal forming processes [7]. The energy dissipation associated with the nucleation and growth of voids and micro-cracks caused by the plastic flow has a dominant effect, suggests the coupling between plastic flow and damage at the constitutive level [8].

In turn, the establishment of the constitutive laws that are capable of modelling the material behaviour/degradation plays a major role in industrial machines or products dimensioning. That is, the precise prediction of deformation and failure allows efficient designs and optimisation solutions for a given product or machine, saving financial resources [8].

Most of the industrial parts fail due to fatigue, that is, under repeated cyclic loading, and a considerable amount of literature in the subject is available nowadays [9–11]. The traditional approach to fatigue is based on experimental relations between the loss of resistance of the material and the number of cycles, such as the Wohler curves. In general, experimental curves are obtained for specific loading conditions and values are extrapolated for particular parts and loading scenarios. Plasticity effects may also be incorporated making use of the Manson [12] and Coffin [13] semi-empirical relations. Alternatively, fracture might be related to fracture models such as the Paris law. The partial

crack closure effect appears when the crack is compressed or subjected to shear stresses. The closure effect is very important in complex strain paths situations because it allows better approximations of the experimental results. Under a cyclic loading, metals exhibit the so-called Bauschinger effect, characterised by a decreased resistance to plastic yielding when charged in two opposite directions. This effect may be modeled through kinematic hardening, as introduced by Chaboche in the original Lemaitre model [14–16]. Here kinematic hardening is equally introduced in the Lemaitre model using an internal variable approach, a strain-like variable, in line with reference [17].

The theory of Continuum Damage Mechanics (CDM) assumes the existence of a internal material damage variable that participates in the dissipative processes. Plasticity and damage are then strongly coupled within this approach. The standard CDM theories assumes that the material is homogeneous and continuous at any size scale, however, this assumption is not valid when deformation reaches a critical level. Experimental observations shows that the internal degradation of the material leverage the macro-structural response to external loads. Moreover, plastic strain tends to concentrate in a localised zone while the body experiences a global strain-softening regime. At this stage the defects in the micro-structure play a crucial role and are the main responsible for the onset of the failure phenomenon [8].

From a numerical point of view, the damage evolution description using the local theory leads to a mesh dependent solution. In classical multi-variable calculus, the static (dynamic) problems partial differential equilibrium equations are classified as elliptic (hyperbolic). As long as these equations remain elliptic (hyperbolic) the solution of the static (dynamic) Initial Boundary Value Problem (IBVP) is guaranteed to be unique. However, in the softening stage, the material tangent modulus becomes negative and the ellipticity (hyperbolicity) is lost and uniqueness of solution disappear. This lack of ellipticity (hyperbolicity) leads to a pathological dependence of the solution on the spatial discretization when using numerical methods. Another suitable approach, which is used on this thesis to compare with local models, is the so-called Non-Local Formulation (NLF). The NLF incorporates an intrinsic length into the classical continuum theory by employing spatially weighted averages through an integral operator [8]. Regardless the advantages of the non-local formulation of the damage variable this dissertation only includes its local formulation.

The numerical techniques for the simulation of the solids behaviour, usually based on the Finite Element Method (FEM), are used by a growing number of designers. These techniques have achieved, in many areas, a high degree of security and constitutes an essential project tool [18]. Despite the great advances made in simulations which involved various materials under a wide range of circumstances, the behaviour description is far from being solved. In general, the models are nonlinear and the solids are subject to large deformations. For many industrial applications, description of the material response using conventional models may lead to a poor description of the actual process. Therefore,

despite the fundamental differences between the nature of the microscopic mechanisms of damage and elasto-plastic processes, the classical theory of plasticity has been extended beyond its limits of applicability and used to describe materials whose behaviour is mostly dominated by an internal damage evolution [4].

Using the Continuum Damage Mechanics (CDM) principles it is possible to describe in a phenomenological way the microscopic deterioration of a material based on a thermodynamic framework. Ductile materials usually presents moderate to large plastic deformations before the macro crack initiation. Plastic strains may result from crystalline slip through dislocation motion or from degradation of the mechanical properties and therefore both mechanisms are strongly coupled in this type of materials. The appropriate modelling of ductile damage, which is crucial to describe the deformation of metals undergoing large deformations, has been the focus of extensive research.

Since the initial concepts of CDM [19] several contributions have emerged in order to describe the material progressive degradation [6, 20, 21].

In the model proposed by Lemaitre [6], the material progressive degradation is treated as an internal variable, acting in an averaging sense within a representative volume (RVE), which size is in accordance to a scale where the material may be considered as homogeneous. It describes the mechanical properties degradation before the formation of macro cracks, and the analysis may pass through the elastic, plastic-hardening and plastic-softening stages of material response. Basically, the internal damage can be defined by the presence and evolution of cracks and cavities at the microscopic level that can eventually lead to complete loss of load capacity of the material.

The characterisation of the internal injury as well as the scale at which this occurs in the common engineering materials crucially depends on the type of material in question. Furthermore, for the same material, the evolution of damage can be activated by very different physical mechanisms and depends fundamentally on the type and loading rate, temperature, and environmental factors such as exposure to corrosive substances or nuclear radiation [18].

1.1.2 Isogeometric Analysis

Computational analysis of human made or natural objects became increasingly important in industrial applications and processes during the recent 20 years. In this respect, objects can be characterised by setting the boundary conditions and the applied forces into a material object. For example an object can be, the study of a suspension subjected to fatigue solicitation or the study of a fluid-structure interaction problem like the effects of a gust of wind on a pedestrian bridge or the friction-related turbulences of the artery blood flow. So, the object of study is related to an specific strand of many problems and solutions developed in FEA researches: solid mechanics, fracture mechanics, electromagnetics, heat transfer, manufacturing processes, and others. The combination of the physics involved by systems of partial differential equations and geometric description has promoted better

and more efficient methods for solving mathematical problems numerically. This work was driven by the existing gap between Finite Element Analysis (FEA) and computer-aided design (CAD). Bridging these two tools it is even necessary to unify analysis and design fields. It would be of great advantage if there was interoperability between these two systems to facilitate computational analysis and engineering processes. That is the main goal of Isogeometric Analysis (IGA). In future, numerical computational simulations using IGA concept should provide accurate results and facilitating all the process.

Whereas CAD systems are characterised by "exact" (small gaps within predefined tolerances are allowed) descriptions of the inner and outer shells of the object and 3D models are sufficiently accurate for production purposes In FEA the object is represented with a description of composed structures of finite elements, where there is a cruder representation of the shape of inner and outer hulls. In addition FEA needs compact geometric descriptions, where unnecessary detail is removed to focus the analysis on essential properties of the objects, namely, the simulation is performed only in the regions of interest to study the physical problem.

Right now, numerical simulation often involves using the Finite Element Method (FEM) where the geometry model, derived from CAD, usually will suffer a reparameterization of the CAD geometry by piecewise low order polynomials (mesh), generally applying linear Lagrange polynomials to approximate the geometry. This information transfer between models suitable for design (CAD) and analysis (FEM) is considered being a bottleneck in industry (industrial applications) of today, because it introduces significant approximation errors, or makes the simulations computational costly in FEM models with fine mesh, and entails a huge amount of man-hours to generate a suitable finite element mesh.

Nowadays most CAD systems use spline basis functions and often Non-Uniform Rational B-Splines (NURBS) of a different polynomial order. For that reason, IGA is based on NURBS, where the main idea is to use the same mathematical description for the geometry in the design process within CAD and the numerical procedures used in FEA simulations. In other words, IGA is characterised by the use of a common spline basis for geometric modelling and Finite Element Analysis of a given object and can be considered a generalisation of FEM analysis. Much research in application of IGA have been done at various topics of FEA: linear and non-linear static and dynamic analysis of thin-walled structures, fluid mechanics, fluid structure interaction, shape and topology optimisation, vibration analysis, buckling and others.

Isogeometric analysis based on NURBS (Non-Uniform Rational B-splines) was introduced by Tom Hughes [22] and further expanded in [23]. The objectives of IGA are to generalise and improve upon FEA in the following ways:

- Get volumetric spline models having the expected behaviour according to the Partial Differential Equations system (PDEs) and according with boundary conditions and loads behind the physical phenomena in analysis;

- Represent common engineering shapes (circles, cylinders, spheres, ellipsoids, etc.) and provide accurate modeling of complex geometries. This means that geometrical errors optimally should be eliminated;

- Simplify mesh refinement of geometries by eliminating the need for communication with CAD geometry once the initial mesh is constructed;

- Provide systematic refinements (h, p and k refinements) that exhibits improved accuracy and efficiency compared with classical FEA.

However, since this is a recent method there are some challenges to overcome. Currently the CAD systems are programmed to define precisely the models geometry through surfaces but, in a general case, the FEM uses volume elements . The creation of a volumetric spline model from the surfaces of the CAD model suggests the study of local refinement techniques.

On one side the main quality criteria for CAD systems are face connectivity and shape accuracy suitable for production processes. Today these requirements are achieved through NURBS surfaces. On the other side, an FEA system is characterised by volume block connectivity and model refinement in critical regions (local refinement). Nowadays that is achieved by the use of structures of trivariate parametric polynomials [24].

At this point, we can ask why the combination of FEM and the use of splines did not happen earlier. One possible reason is that mathematical representations in CAD and FEA were chosen based on what was computationally feasible in the early days of the technology development. While CAD developed to improve the design process FEM developed to improve analysis in engineering. A rigorous mathematical foundation of FEA was given around 1970. The publication [25] is one example of many publications published with that purpose. De-Boor-Cox calculation (1972) and Oslo Algorithm (1980) are stable algorithms to generate B-Splines and they were introduced, as you see, after FEM developments.

In the course of time, the gaps between CAD and FEA technologies increased and it has become more and more difficult to maintain the compatibility between these two systems.

Today in FEA, designers generate CAD model files that often includes ambiguities (gaps and overlaps, and levels of detail such individual bolts and welds). These ambiguities must be removed to arrive at an Analysis Suitable Geometry (ASG)[1] that is suitable for the use in a particular type of analysis. After this step, using sample points of an ASG surface, the surface mesh is created [26]. Notice that this stage is considered an bottleneck because, at some complex geometries, it can take 80% of the overall analysis time to create this ASG mesh. Also the mesh is created from a CAD surface with a trivariate representation by a transformation to polynomials of a lower degree, most often of degree 1 or 2. Thus

[1] geometric description that is satisfactory for the problem of interest.

there will occur only shape approximations of the CAD models during this transformation process, because those polynomials of lower degree cannot represent complex shapes like curved surfaces (ellipsoids for example) accurately, in the general case [27].

After generating and refining critical zones of the surface mesh, the process proceeds to volume meshing, and if any typical error occur at this stage it's needed to simplify the surface mesh. Also it is defined boundary conditions. The simulation is run and then comes the stage of post-processing phase, which consists in analysing the resulting graphic models. The whole process is described in figure 1.1. The development of global and local refinement techniques will allow improving the accuracy and efficiency of the method [28].

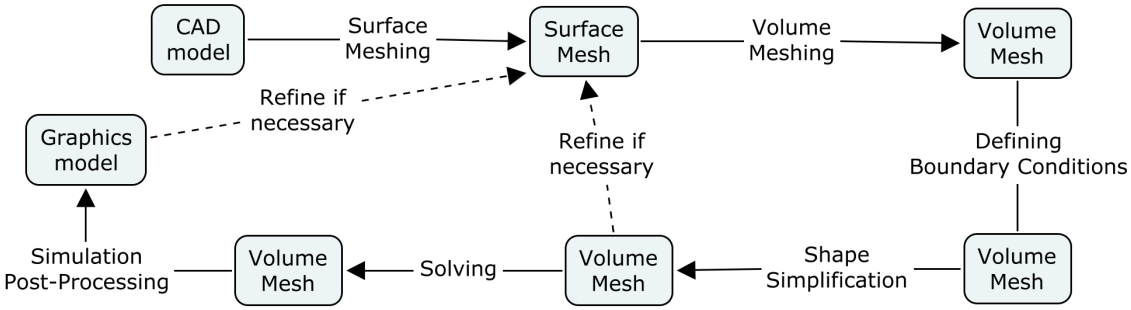

Figure 1.1: Traditional simulation pipeline [1].

In the future it is intended that the designing process of a model and its simulation occur in the same product. The process can start from CAD shape model done by the designer or from an "As-is" model[2]. Both base models are twovariate splines models and it will be required to create an Isogeometric CAD model suitable for analysis, that is a trivariate rational spline model. After that, unnecessary details can be removed (Simplified Isogeometric model) and the model undergo a process of local refinement (meshing[3]). After this step the process has the same steps of FEA: set boundary conditions, solving and run the simulation, and direct visualisation of the results. Figure 1.2 shows the main steps of process analysis with isogeometric technology.

Analysing figure 1.2 we can find some challenges to implement this process in an "user friendly way". Namely, the goal is to have an automated process from the first step until the last.

The first challenge is the creation of an "as-is" model. CAD models combine elementary surfaces (plane, cone, cylinder, sphere, torus and NURBS), aimed at visual purposes. Extracting information from, for example, laser scanning and using the datasets for validation and updating 3D-CAD-models is challenging. This topic is very important, because

[2]This type of model is obtained directly from Image Processing and Data Visualisation techniques (laser scan for example). Built for the purpose to obtain a model as realistic as possible

[3]Note that isogeometric meshing approach differs from FEA. In isogeometric meshing the geometry remains the same but some splines of the model are better suited to describe deformations gradients. We will see some methods to do that in chapter 2.

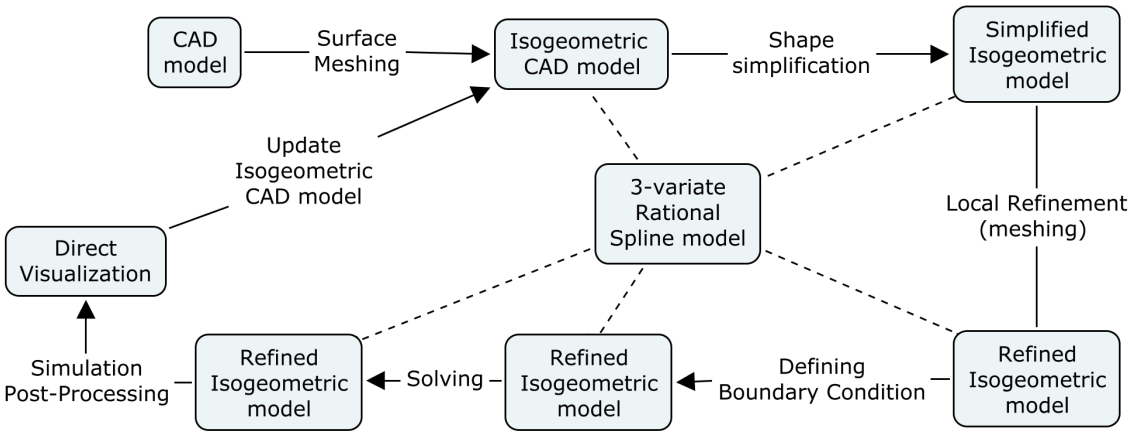

Figure 1.2: Possible information flow using Isogeometric concept [1].

in order to create a model as realistic as possible, we must use locally refined splines. However, the process can be started with a CAD model created from an adequate software.

The second challenge is the creation of trivariate isogeometric model. "As-is" or CAD shape models mathematically only describes the inner and outer hulls, the isogeometric model is analysis/simulation suitable and describes the volumes mathematically by watertight structures of blocks of trivariate rational splines. Building an isogeometric model is a challenge, because there is a mismatch between the surface patch structure of the source model, and a suited block structure of an isogeometric trivariate rational spline model. It's necessary to use locally refined splines for this stage as well.

The next challenge is the isogeometric analysis itself. Basically, the method replaces traditional finite elements by NURBS, the representation of shape is more accurate, allows higher order methods, performing much better that traditional finite elements and allowing refinement of models without remeshing. But, augmented spline technology like locally refined splines is needed, to cover all possible model geometries.

The last challenge resides in isogeometric visualisation (post-processing phase). Current visualisation technology, as already mentioned, addresses low order elements and results are degraded and also involves loss of information. It is evident that exploiting higher order representations can better represent singularities (regions of model with high gradients of deformation) in the solution.

These last challenges relies on all phases of the modelling processes: pre-processing, processing, and post-processing. Since the origin of isogeometric technology several contributions have emerged in many areas of all modeling phases. The following topics will reveal an overview of some literature about isogeometric technology so far [27, 29]:

- **Shape Optimization Problems**: The tight coupling between CAD and FEA models reveals an attractive approach for shape optimization, that is, the control variables of the geometry provide a well stablished parameterization that can be used

as design variables ([30–33]). The main idea is once an optimal design is achieved, it can be returned to the CAD system. Elements that require only a boundary discretization creates a direct coupling with CAD. Boundary element methods for elastostatic analysis were presented in [34, 35].

- **Alternative Geometry Discretizations**: From an analysis view, the NURBS tensor product structure is inefficient because the global nature of refinement operations. In turn, this leads to inefficient error estimation and adaptivity algorithms. The use of T-splines [36] overcome the limitations of NURBS. T-splines correct the deficiencies of NURBS by creating a single patch, watertight geometry which can be locally refined and coarsened. Several type of splines have been developed in order to perform better and suitable meshes types [37–57].

- **Contact Mechanics**: The faceted surfaces of FEA typical discretization leads to stresses surges or remoteness, unless fine meshes are used. However, smooth contact surface are obtained using NURBS, leading to more physically accurate contact stresses. Recent work in this field includes [58–62].

- **Plates and Shells Formulations**: Shells and plates problems are another field where IGA has a huge potential [63–69]. The smoothness of the NURBS allows for a straightforward construction of plate/shell elements. For example, thin shells rotation-free formulations can be easily constructed, exhibiting less pronounced shear-locking compared to standard FE plate/shell elements, and elements with smooth boundaries also were successfully constructed [70, 71].

- **Fluids and Fluid-Structure Interaction Problems**: Once again, the NURBS smoothness is also attractive for fluids and fluid-structure interaction analysis [72–76].

- **Phase-field modelling**: Due to the ease of constructing high order continuous basis functions, solving PDEs of fourth or higher order derivatives of the field variable is another interesting research field [77–80].

- **Structural Vibrations**: NURBS also provide advantageous properties for structural vibration problems [81–84] where IGA k-refinement provide more robust frequency spectrum than higher-order p-elements from FEA.

- **Fracture Mechanics**: IGA has been applied to cohesive fracture, Linear Elastic Fracture Mechanics (LEFM) [85], dynamic fracture and delamination of composite laminates. Also, a continuum description of fracture using explicit gradient damage models was studied using NURBS [77].

- **Computational Aspects**: Some computational aspects about IGA have been studied so far,

1. Unfortunately NURBS based analysis are not free locking. Locking removal techniques were applied to IGA in [86–89].
2. The use of higher-order NURBS functions minimize the impact of the mesh distortion [90].
3. The typical NURBS high order basis functions usually introduces higher computational costs in comparison with the typical FE methods. The performance of direct solvers as analysed in [91]. In order to minimize this problem collocation methods have been developed [92, 93].
4. The mesh quality is provided by the quality of the geometry parametrisation used.
5. Get volumetric models from CAD representations of a solid demands several conversion steps. Initial developments have been published in [1]. Note that with boundary elements developed in [34, 35] the analysis is performed through a surface model.
6. Numerical Integration techniques: Gaussian quadrature is not optimal for IGA. However, nearly ideal integration techniques have been presented on [94, 95].

1.2 Motivation and Goals

In this work it is intended to contribute to the analysis of forming processes and pipeline applications by discussing the use of an isogeometric approach.

The primary goal of this dissertation is the development of computer models for the simulation of ductile material subjected to monotonic and cyclic loads, based on the Finite Element Method and Isogeometric discretization type. For the enjoyment of this fundamental goal, the work involved the following set of partial objectives:

- Develop constitutive laws for a fully coupled continuum mechanics models using isogeometric elements;
- Modelling of material behaviour through some introductory examples;
- Validation of the results by comparison with FEM models results;
- Conclude about the results exposing the limitations and advantages of the approach used along this work;

In this thesis, a previous finite element elasto-plastic models with isotropic, kinematic hardening, and with the damage effects were extended in order to include the proper isogeometric discretisation. Such an extension is obtained by incorporating the Non Uniform Rational B-Splines as the basis functions. The discretisation was performed taking the advantages of the symbolic interface of AceGen systems. The AceGen software

provides an environment for designing and implementing numerical code throughout a symbolic-numeric interface [96]. It contains several techniques with the symbolic and algebraic capabilities of *Mathematica*: automatic differentiation, automatic code generation, simultaneous optimisation of expressions, and theorem-proving via stochastic evaluation of expressions.

1.3 Dissertation Outline

Chapter 2 of this thesis is devoted to gives an overview of the NURBS-based isogeometric analysis framework. The concept of B-spline polynomials and NURBS are introduced, focusing only on basic definitions, construction of solution spaces, refinement algorithms, and geometrical modelling approaches.

In its turn, the Chapter 3 of this dissertation gives an overview of Continuum Damage Mechanics (CDM) principles. Starting with the kinematics description, the main tensors and its physical meaning are exposed, the conservation principles are applied and the basis for the develop of constitute models is studied. With the conceptts developed on the previous chapter, Chapter 4 focus on the definition of potential functions and on the deformation mechanisms.

The Chapter 5 includes the discretisation and some guidelines related to the AceGen implementation code. Finally, Chapter 6 validate the developed models trough some numerical examples and Chapter 7 includes some final remarks and references to future works.

Chapter 2

Pre-analysis Tools for IGA

This chapter focus on geometric design based on NURBS and depicts some features about its mathematical properties and finite element computational implementation.

2.1 Introduction

In order to describe complex curves, surfaces or solids, parametric representations are used. NURBS parameterization is well suitable to describe the geometry of the model. A curve, surface, or solid can be described parametrically, respectivelly, as

$$\mathbf{C}(\xi) = (x(\xi), y(\xi), z(\xi)), \qquad (\xi) \in [0,1] \tag{2.1}$$

$$\mathbf{S}(\xi,\eta) = (x(\xi,\eta), y(\xi,\eta), z(\xi,\eta)), \qquad (\xi,\eta) \in [0,1]\times[0,1] \tag{2.2}$$

$$\mathbf{G}(\xi,\eta,\zeta) = (x(\xi,\eta,\zeta), y(\xi,\eta,\zeta), z(\xi,\eta,\zeta)), \qquad (\xi,\eta,\zeta) \in [0,1]\times[0,1]\times[0,1] \tag{2.3}$$

The use of polynomials as a tool for computational modeling of geometric entities can approximate a large number of functions and these kind of functions are easily differentiated and integrated.

Several developments were made in order to develop well posed functions to describe complex geometries. First, Bernstein polynomials emerged [97]. Later, Bézier parameterization employing Bernstein polynomials allowed the parametric description of a curve, surface or solid. But, complex geometric entities cannot be represented using just one polynomial function to define the entire domain. It is then that emerges the idea to split the domain of the geometric entity (curve, surface or solid) into subdomains. Therefore,

polynomials by parts have been employed to describe the geometric entities, where breakpoints are enforced up to some desired continuity order and are the end points for every subdomain. Note that these breakpoints are related to the knot vectors of the respective curve, surface or solid, in each direction. The B-spline and NURBS basis functions definitions contains this subdomain approach and are mathematically representations of 3D geometry that can accurately describe any shape from a simple 2D line, circle, arc, or curve to the most complex 3D free-form surface or solid. [97]

With NURBS a modeling system can use a single internal representation for a wide range of curves and surfaces (straight lines, flat planes, circles, spheres, even free-form surfaces), that is the key to developing a robust modeling system. As a result, NURBS are the standard of much of the computer aided design (CAD) and interactive graphics community [98].

This chapter is intended to understanding the fundamental of isogeometric analysis and NURBS, demystifying some mathematics required. First, it is important addresses main concepts involved in this theory. After that, will be developed the theory beyond B-spline curves, surfaces and solids and some fundamental tools like h, p and k refinements. The comparison with FEA will be made whenever necessary.

2.2 Isogeometric Analysis Approach

In FEA an element has two representations, one in the parent domain and one in the physical space. Their nodal coordinates and the degrees-of-freedom (the values of the basis functions at the nodes) define an element. With the isoparametric concept a set of elements defines the geometry, also called mesh. The basis functions[1] are interpolatory and may be positive or negative in their domain.

In NURBS, there are two notions of meshes: the control mesh and the physical mesh. The degrees-of-freedom are located at the control points and control points define the control mesh. So, the control mesh interpolates the control points and consists of multilinear elements and isn't the actual geometry. We can change the control mesh for numerical quadrature purposes and the physical geometry may still remain valid (in contrast to the finite element approach).

The physical mesh is a decomposition of the actual geometry. The elements in the physical mesh are represented by patches and knot spans. The patch can be seen as a macro-element or subdomain. Each patch has two representations, one in a parent domain and one in physical space.

Each patch can be decomposed into knot spans, that are the smallest entities that we deal with. Knot spans are bounded by knots. Knots are points, lines or surfaces, depending if the problem is, respectively, in one-, two-, or three-dimensions. The knots define knot span domains (which can be regarded as element domains of FEA) where basis

[1] also called interpolation functions or shape functions.

functions should be smooth. Across knots, basis functions will be C_{p-m} where p is the degree of the polynomial and m is the multiplicity of the knot in question [2]. Logically, knot spans also have representations in both a parent domain and physical space.

Another important notion that is a key to understand the functionality of NURBS is the index space of a patch. It uniquely identifies each knot and discriminates among knots having multiplicity greater than one [27].

2.3 B-Splines and NURBS

NURBS are built from B-splines. Unlike in standard FEA, the B-spline mapping is local to patches [3] rather than elements. The parameter space in FEA is mapped into a single element in the physical space, and each element has its own such mapping. On the other side, the B-spline mapping is global to the whole patch rather than to the elements themselves, which takes a patch of multiple elements in the parameter space into the physical space. Besides that, each element in the physical space is the image of a corresponding element in the parameter space. The NURBS mapping will be defined in next sections.

2.3.1 Knot Vectors

The knot vector is a set of numerical values describing the knot coordinates in the parametric space, where non-decreasing sequence of parametric coordinates, $\xi_i \leq \xi_{i+1}$, $i = 1, \ldots n+p$. The ξ_i are called knots. Depending on the geometric topology, knot spans may represent points, lines or surfaces. After the knot coordinates are established, the knot spans are always surrounded by two consecutive knots, constituting the elementary entities for Isogeometric Analysis in the same manner as elements are basic entities for Finite Element Analysis (FEA).

If the the order of the polynomial basis functions is p, the parametric coordinates at the beginning and at the end of an open knot vector are repeated $p+1$ times, and internal knots may be repeated p times. Open knot vectors are the most used by the geometric modeling packages. Each time a internal knot is repeated the continuity of the curve will decrease by one at respective control point. The basis functions are interpolatory at the end knots and in internal knots that have multiplicity p (repeated p times). This is distinguish feature between knots and nodes in FEA because FEA elements are interpolatory.

The B-spline basis functions are defined by Cox-de-Boor recursion formula (Cox, 1971; de Boor, 1972) for a given knot vector (Ξ, $\mathcal{H}$ and $\mathcal{Z}$) which are defined over the parametric space, the number of control points (n, m and l) and the polynomial degree (p, q and r) and over respective direction of the parametric space (ξ, η and ζ).

[2] This question will be mathematically defined at section 2.3

[3] subdomains with well defined element types and material.

So B-spline basis functions are defined as [97]

$$N_{i,p}(\xi) = \frac{\xi - \xi_i}{\xi_{i+p} - \xi_i} N_{i,p-1}(\xi) + \frac{\xi_{i+p+1} - \xi}{\xi_{i+p+1} - \xi_{i+1}} N_{i+1,p-1}(\xi) \tag{2.4}$$

over the knot vectors in respective directions

$$\begin{aligned} \Xi &= \{\xi_1, \ldots, \xi_{p+1}, \ldots, \xi_{n+1}, \ldots, \xi_{n+p+1}\} \\ \mathcal{H} &= \{\xi_1, \ldots, \eta_{q+1}, \ldots, \eta_{m+1}, \ldots, \eta_{m+q+1}\} \\ \mathcal{Z} &= \{\xi_1, \ldots, \zeta_{l+1}, \ldots, \zeta_{r+1}, \ldots, \zeta_{r+l+1}\} \end{aligned} \tag{2.5}$$

starting with piecewise constants ($p = 0$)

$$N_{i,0}(\xi) = \begin{cases} 1, \xi_i \leq t \leq \xi_{i+1} \\ 0, otherwise \end{cases} \tag{2.6}$$

In addiction, B-spline geometries can be seen as a linear combination of B-spline basis functions presenting minimal support with respect to a given degree, continuity and domain partition.

At this point we can address some features and include an introductory example about the NURBS when used as shape functions into isoparametric concept. First, the B-spline mappings start from the parameter space whereas the parent space. This means that, each patch on the parameter space (subdomains comprised of many knot spans) is mapped into a single element in the physical space. On the other side, in FEA each element in the parent space is mapped into a single element in the physical space. Figure 2.1 shows the differences for a two-dimensional problem.

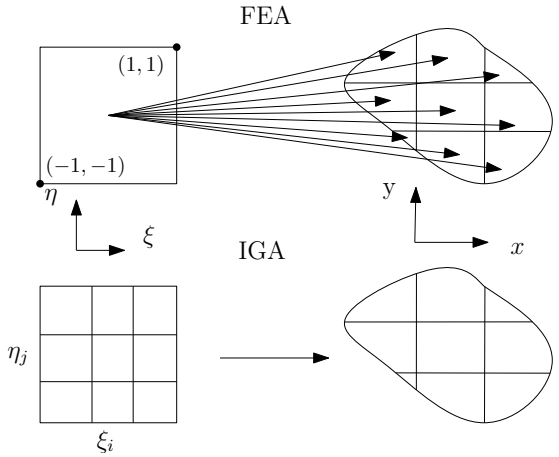

Figure 2.1: Isoparametric concept applied for both FEA and IGA approaches.

Setting $p = 2$ and an open non-uniform knot vector $\Xi = \{0,0,0,1,2,3,4,4,5,5,5\}$ we obtain the shape functions, presented in Figure 2.2, in the parameter space.

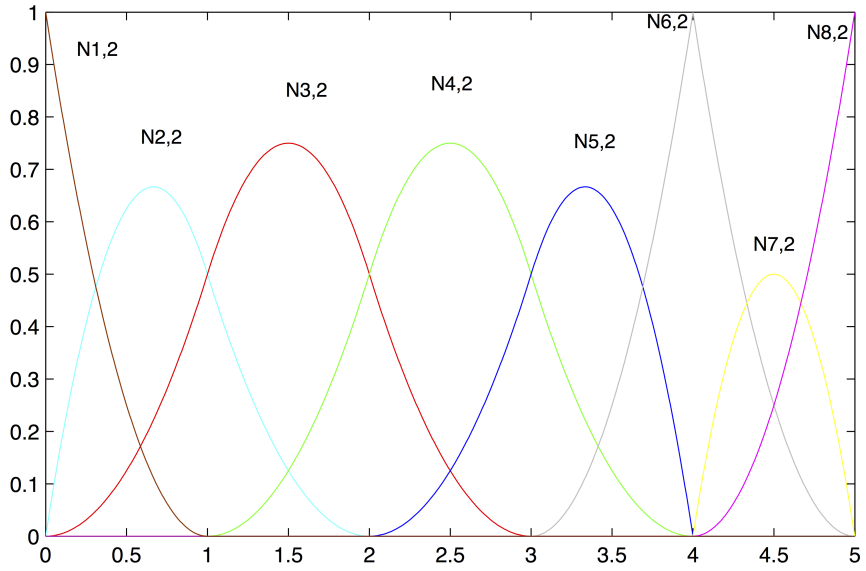

Figure 2.2: Quadratic basis functions for the open non-uniform knot vector $\Xi = \{0,0,0,1,2,3,4,4,5,5,5\}$.

In this example, the first and last knots are repeated three times because the shape functions are quadratic. In addition, the knot 4 is repeated two times, leading to a interpolation condition in the respective knot.

Hughes et al. [22] and Cottrell et al. [27] addressed the most fundamental properties of the basis functions. These properties are very important in IGA

1. Basis functions form a partition of unity, that is

   $$\sum_{i=1}^{n} N_{i,p}(\xi) = 1 \ , \ \xi \in [\xi_1, \xi_{n+p+1}]$$

2. The support of each $N_{i,p}(\xi)$ is compact and contained in $[\xi_i, \xi_{i+p+1}]$

3. The basis functions are non-negative, that is, $\forall \xi \rightarrow N_{i,p}(\xi) \geq 0$

2.3.2 NURBS solids

For one-dimensional knot vector $\Xi = \{\xi_1, \ldots, \xi_{n+p+1}\}$, a B-spline curve $\mathbf{C}_p(\xi)$ in $\mathbb{R}^3$ of order p is obtained by linear combination of the basis functions having as coefficients the coordinates of n control points $\mathbf{P}_i$. The mathematical expression is

$$\mathbf{C}_p(\xi) = \sum_{i=1}^{n} N_{i,p}(\xi)\mathbf{P}_i \tag{2.7}$$

A B-spline surface is constructed from a net of control points $\{\mathbf{P}_{i,j}\}$ and from a two-dimensional knot set $\Xi \times \mathcal{H}$. The knot vector $\mathcal{H} = \{\eta_1, \eta_2, \ldots, \eta_{m+q+1}\}$ of degree q have

m control points or basis functions along the η direction. So, a tensor product B-spline surface is defined as

$$\mathbf{S}_{p,q}(\xi,\eta) = \sum_{i=1}^{n}\sum_{i=1}^{m} N_{i,p}(\xi)N_{j,q}(\eta)\mathbf{P}_{i,j} \tag{2.8}$$

In its turn, a tensor product B-spline solid are defined in analogous fashion. Given a control net $\{\mathbf{P}_{i,j,k}\}$ and three-dimension knot set $\Xi \times \mathcal{H} \times \mathcal{Z}$, where $\mathcal{Z} = \{\zeta_1, \zeta_2, \ldots, \zeta_{l+r+1}\}$ is a knot vector of degree r with l control points or basis functions along the ζ direction, is defined as

$$\mathbf{G}_{p,q,l}(\xi,\eta,\zeta) = \sum_{i=1}^{n}\sum_{j=1}^{m}\sum_{k=1}^{l} N_{i,p}(\xi)N_{j,q}(\eta)N_{k,r}(\zeta)\mathbf{P}_{i,j,k} \tag{2.9}$$

The rationalization of B-Splines involves a definition of a new basis functions, constructed from B-Spline basis functions. To define these rational basis functions is associated a weight w to a control point. So, a NURBS curve is defined by

$$\mathbf{C}_p(\xi) = \sum_{i=1}^{n} R_{i,p}(\xi).\mathbf{P}_i \tag{2.10}$$

where ${R^p}_i$ is the NURBS basis functions for a curve and it's mathematical expression is

$${R^p}_i(\xi) = \frac{N_{i,p}(\xi)w_i}{\sum_{i=1}^{n} N_{i,p}(\xi)w_i} \tag{2.11}$$

where w_i is the weight of control point $\mathbf{P_i}$.

Following the same reasoning, NURBS surfaces and solids are defined, respectively, by

$$\mathbf{S}_{p,q}(\xi,\eta) = \sum_{i=1}^{n}\sum_{j=1}^{m} R_{i,j}^{p,q}(\xi,\eta)\mathbf{P}_{i,j} \tag{2.12}$$

$$\mathbf{G}_{p,q,l}(\xi,\eta,\zeta) = \sum_{i=1}^{n}\sum_{j=1}^{m}\sum_{k=1}^{l} R_{i,j,k}^{p,q,r}(\xi,\eta,\zeta)\mathbf{P}_{i,j,k} \tag{2.13}$$

where rational basis functions are defined by the following equations

$$R_{i,j}^{p,q}(\xi) = \frac{N_{i,p}(\xi)N_{j,q}(\eta)w_{i,j}}{\sum_{i=1}^{n}\sum_{j=1}^{m} N_{i,p}(\xi)N_{j,q}(\eta)w_{i,j}} \tag{2.14}$$

$$R_{i,j,k}^{p,q,l}(\xi,\eta,\zeta) = \frac{N_{i,p}(\xi)N_{j,q}(\eta)N_{k,r}(\zeta)w_{i,j,k}}{\sum_{i=1}^{n}\sum_{j=1}^{m}\sum_{k=1}^{l} N_{i,p}(\xi)N_{j,q}(\eta)N_{k,r}(\zeta)w_{i,j,k}} \tag{2.15}$$

Additional information on NURBS may be found in [97]. As a comment to the previously equations, NURBS can be considered as a mapping from parametric space $\hat{\Omega}$ to

physical space Ω. The definition for the mapping from parametric space to the physical space will be made in section 2.4.2.

2.4 Main features of IGA and comparison with FEM

This section aims to show the differences and similarities between IGA and FEM.

Trivariate discretisations defined by 2.13 are not given in a explicitly way and usually some preprocessing is required before the application of the numerical solution. IGA and FEA are both isoparametric implementations of Galerkin's method, thus the code architectures are very similar [29].

2.4.1 Relevant spaces

For the use of NURBS as a basis for analysis it is important to define the mappings and the spaces.

2.4.1.1 Index space

The index space consists of a net of index knot points for all combinations of the NURBS patch, regardless of whether the knot is repeated or not. The index space is illustrative for analyzing the support of the basis functions, which can easily be read in this space, but are less apparent in the parametric space. Figure 2.3 shows a bivariate NURBS patch represented at the index space.

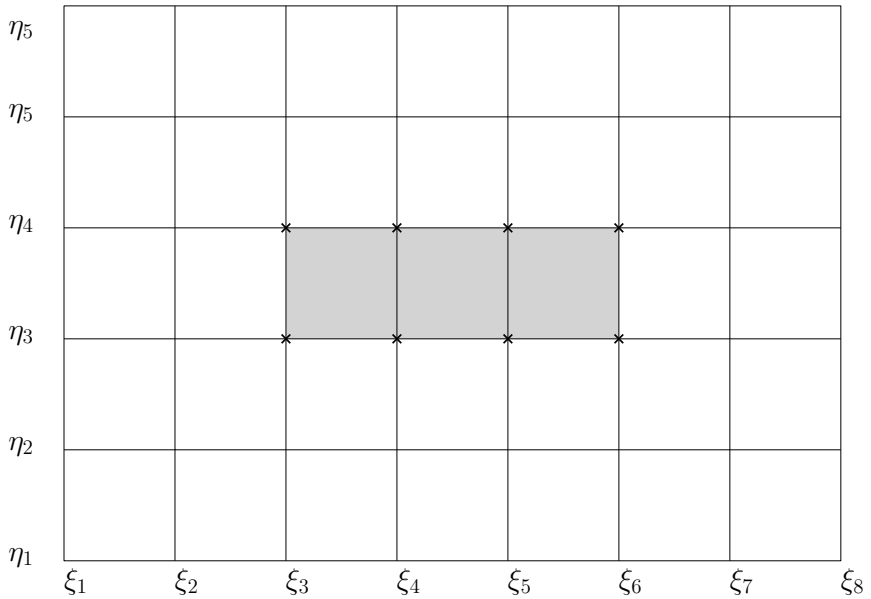

Figure 2.3: Bivariate NURBS patch on index space containing the parameter space (gray filled).

2.4.1.2 Parameter space

Parametric space (the pre-image of the NURBS mapping) is formed by only the non-zero intervals between knot values forming the parametric space $\hat{\Omega} \subset \mathbb{R}^{d_p}$ $(d_p = 1,\ 2,\ 3)$ associated with a set of parametric coordinates $\boldsymbol{\xi} = (\xi, \eta, \zeta) = (\xi^1, \xi^2.\xi^3)$.

Regarding the attention to figure 2.3, the region bounded by knot lines with non-zero area contains a set of unique knot values δ such that δ is the element domain. More formally, a set of ${n_s}^i$ unique knot values δ^i in the parametric direction i such that

$$\delta^i = \left\{ {\xi_1}^i, {\xi_2}^i, \cdots, {\xi_{{n_s}^i}}^i \right\}, \quad {\xi_j}^i \neq {\xi_j}^i \tag{2.16}$$

represents the unique knot values for each parametric direction i. So, a generic element is defined in a multivariate case by

$$\hat{\Omega}^e = [\xi_i, \xi_{i+1}] \otimes [\eta_j, \eta_{j+1}] \otimes [\zeta_k, \zeta_{k+1}], \quad 1 \leq i, j, k \leq {n_s}^1, {n_s}^2, {n_s}^3 - 1 \tag{2.17}$$

for the knots that are unique, that is, $\xi_i \in \delta^1$, $\eta_j \in \delta^2$, $\zeta_k \in \delta^3$, and n_s^i is the number of unique knots along parametric direction i. A possible numbering scheme for elements over a patch is

$$e = k\left({n_s}^2 - 1\right)\left({n_s}^1 - 1\right) + j\left({n_s}^2 - 1\right) + i \tag{2.18}$$

2.4.1.3 Physical space

The NURBS mapping transform coordinates in parameter space to the physical space $\Omega \subset \mathbb{R}^{d_p}$. For trivariate domains, a coordinate system $\mathbf{x} = (x, y, z) = \left(x^1, x^2.x^3\right)$ is associated for the physical space.

Note that neither the index knots in the index space nor the parameter space are directly linked with control points on the physical space.

2.4.1.4 Parent space

The previous three spaces are inherent to NURBS but to perform the analysis routines it is required the definition of an additional space, the parent space $\tilde{\Omega}^e = [-1, 1]^{d_p}$. Parent space is used for numerical integration routines which are often defined over the interval $[-1, 1]$ and the respective coordinates are denoted as $\tilde{\boldsymbol{\xi}} = \left(\tilde{\xi}, \tilde{\eta}, \tilde{\zeta}\right) = \left(\tilde{\xi}^1, \tilde{\xi}^2.\tilde{\xi}^3\right)$.

2.4.2 Discretization

For a given element e, using the isoparametric discrestization, the geometry is expressed as

$$\mathbf{x}^e(\boldsymbol{\xi}) = \sum_{a=1}^{n_{en}} R_a^e(\boldsymbol{\xi}) \mathbf{P}_a^e \tag{2.19}$$

where a is a local basis function index, $n_{en} = (p+1)(r+1)(s+1)$ is the number of non-zero basis functions over the element e, $\mathbf{P}_{i,j,k}$ are the control points and $R_a^e(\tilde{\varepsilon})$ is the NURBS basis function on parent domain associated with index a. The translation of a local basis function index to a global index is made by the connectivity array IEN [27] through

$$A = IEN(a, e) \tag{2.20}$$

Global and local control points are therefore related through $\mathbf{P}_a^e = \mathbf{P}_{IEN(a,e)}$ with similar expressions for R_a^e.

So, the displacement field $\mathbf{u}(\mathbf{x})$ governed by our Partial Differential Equations (PDE) is discretized in a similar manner

$$\mathbf{u}^e(\tilde{\boldsymbol{\xi}}) = \sum_{a=1}^{n_{en}} R_a^e(\tilde{\boldsymbol{\xi}})\mathbf{d}_a^e \tag{2.21}$$

where $\mathbf{d}_a^e$ are the control (nodal) variables.

The discretization process using NURBS introduces the concept of parametric space which is nonexistent in Finite Element simulations. As a consequence, we have an additional mapping in order to operate in parent element coordinates. Usually, there exist a mapping $\tilde{\phi}^e : \tilde{\Omega} \to \hat{\Omega}^e$ that relates parent space and parameter space and a mapping $\mathbf{S} : \hat{\Omega} \to \Omega$ which defines the relation between parameter and physical spaces. The composition $\mathbf{S} \circ \tilde{\phi}^e$ gives the mapping from parent to the physical domain $\mathbf{x}^e : \tilde{\Omega} \to \Omega^e$. Figure 2.4 shows the mappings defined previously.

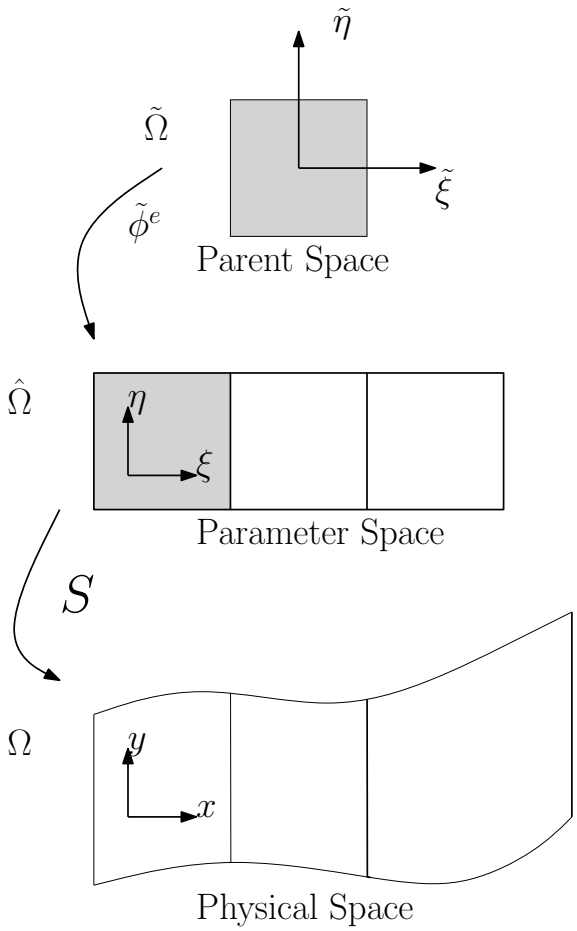

Figure 2.4: Representation of mappings thought from parent space to physical space.

The relation between parent space and parameter space for an element is given by

$$\tilde{\phi}^e\left(\tilde{\tilde{\boldsymbol{\xi}}}\right) = \left\{ \begin{array}{l} \frac{1}{2}\left[\left(\xi_{i+1}-\xi_i\right)\tilde{\xi}+\left(\xi_{i+1}+\xi_i\right)\right] \\ \frac{1}{2}\left[\left(\eta_{i+1}-\eta_i\right)\tilde{\eta}+\left(\eta_{i+1}+\eta_i\right)\right] \\ \frac{1}{2}\left[\left(\zeta_{i+1}-\zeta_i\right)\tilde{\zeta}+\left(\zeta_{i+1}+\zeta_i\right)\right] \end{array} \right\} \tag{2.22}$$

witch associated Jacobian determinant $\left|\mathbf{J}_{\tilde{\xi}}\right|$. In its turn the mapping from parameter space to physical space, given by equation 2.13 for a tridimensional case, leads to a Jacobian matrix (associated with respective Jacobian determinant $|\mathbf{J}_{\xi}|$) given by

$$\mathbf{J}_{\xi} = \left[\begin{array}{ccc} \frac{\partial x}{\partial \xi} & \frac{\partial x}{\partial \eta} & \frac{\partial x}{\partial \zeta} \\ \frac{\partial y}{\partial \eta} & \frac{\partial y}{\partial \eta} & \frac{\partial y}{\partial \zeta} \\ \frac{\partial z}{\partial \zeta} & \frac{\partial z}{\partial \eta} & \frac{\partial z}{\partial \zeta} \end{array} \right] \tag{2.23}$$

obtained performing the following expression

$$\frac{\partial \mathbf{x}}{\partial \boldsymbol{\xi}} = \sum_{a=1}^{n_{en}} \mathbf{P_a^e} \frac{\partial R_a^e(\boldsymbol{\xi})}{\partial \boldsymbol{\xi}} \tag{2.24}$$

where n_{en} is the number of control points of the element.

Since the numerical integration is performed in the parent domain, the Jacobian determinant for the mapping $\mathbf{x}^e : \tilde{\Omega} \rightarrow \Omega^e$ is given by

$$|J| = \left|J_{\tilde{\xi}}\right| |J_{\xi}| \tag{2.25}$$

and the derivatives of basis functions in respect to the physical coordinates are calculated by

$$\left[\frac{\partial {R_a}^e}{\partial \mathbf{x}}\right] = \left[\frac{\partial {R_a}^e}{\partial \boldsymbol{\xi}}\right] {\mathbf{J}_{\xi}}^{-\mathbf{1}} \tag{2.26}$$

Finally, with the mappings previously defined it is possible to integrate a function $f : \Omega \rightarrow \mathbb{R}$ over the physical domain using the parent domain in the following way

$$\int_{\Omega} f(\mathbf{x})\, d\Omega = \sum_{e=1}^{n_{el}} \int_{\tilde{\Omega}} f\left(\tilde{\boldsymbol{\xi}}\right) |J|\, d\tilde{\Omega} \tag{2.27}$$

In this work, the typical Gaussian quadrature procedure was used. It should be emphasised that Gaussian quadrature is not optimal for IGA [29]. Optimal integration procedures have been studied in [94] and [95].

2.5 Concluding Remarks

Along this chapter, the description of the NURBS-based model geometries and the standard of much of the computer aided design, are described in a simplified way. Also, the isoparametric concept used for both FEA and IGA methods is compared.

The main difference between the two isoparametric approaches is that in the isogeometric model we need one additional mapping because the shape functions are defined in the parametric space.

Chapter 3

Standard Continuum Mechanics and Thermodynamics

This chapter reviews the main concepts related to mechanics and thermodynamics of continuum bodies in motion, presented in a more detailed way at [18]. Starting from the description of the main tensors such as such as the deformation gradient, rotations and the different strain measures, and its physical meaning. After that, some stress measures are defined and the conservation principles are applied: mass conservation, momentum balance and the thermodynamics principles. The chapter ends with the basics necessary to formulate the constitutive equations using the thermodynamics with internal variables, neglecting the thermal effects.

In particular, the concepts used to quantify internal straining are of most importance in the formulation of the mechanical and thermodynamical theory of continuum bodies.

3.1 Kinematics

Kinematics provides the basis for motion and deformation description, i.e., describes the motion of an object in the space considering the time dependency. In this section the fundamental quantities employed in the constitutive description of ductile metals are defined.

3.1.1 Motion

Let $\mathbb{B}$ be a deformable solid in region $\Omega \in \mathbb{R}^3$ with the reference configuration defined by $\boldsymbol{X}$. After a given motion or deformation $\mathbb{X}$ within a certain time, the position of an arbitrary particle of the body $\boldsymbol{x}$ is given by

$$\boldsymbol{x} = \mathbb{X}(\boldsymbol{X}, t) \tag{3.1}$$

and is usually referred as the current configuration, at time t. Assuming that the motion $\mathbb{X}$ is invertible, the reference or undeformed configuration $\boldsymbol{X}$ at time t may be recovered

$$\boldsymbol{X} = \mathbb{X}^{-1}(\boldsymbol{x}, t) \tag{3.2}$$

In its turn, the displacement field $\boldsymbol{u}$ is given by

$$\boldsymbol{u}(\boldsymbol{X}, t) = \mathbb{X}(\boldsymbol{X}, t) - \boldsymbol{X} \tag{3.3}$$

and the velocity for a given particle at the position X can be obtained as the time derivative of the motion

$$\boldsymbol{V}(\boldsymbol{X}, t) = \frac{\partial \mathbb{X}(\boldsymbol{X}, t)}{\partial t} \tag{3.4}$$

and the velocity of a particle at the current configuration is obtained by the following way

$$\boldsymbol{v}(\boldsymbol{x}, t) = \boldsymbol{V}^{-1}\left(\mathbb{X}^{-1}(\boldsymbol{x}, t), t\right) \tag{3.5}$$

3.1.2 Deformation Gradient

The deformation gradient is the fundamental kinematic quantity characterizing the changes of each material point during motion. The derivative of the deformation, the Deformation Gradient $\boldsymbol{F}$, is a second order tensor that relates $\boldsymbol{X}$ and $\boldsymbol{x}$ as follows:

$$\boldsymbol{F}(\boldsymbol{X}, t) = \frac{\partial \mathbb{X}(\boldsymbol{X}, t)}{\partial \boldsymbol{X}} = \frac{\partial \boldsymbol{x}}{\partial \boldsymbol{X}} = \nabla_X \mathbb{X}(\boldsymbol{X}, t) \tag{3.6}$$

where ∇_X is generally called material gradient operator. Alternatively, the deformation gradient can also be defined in the current configuration, using the spatial gradient operator ∇_x, as

$$\boldsymbol{F}(\boldsymbol{x}, t) = \left[\nabla_x \mathbb{X}^{-1}(\boldsymbol{x}, t)\right]^{-1} \tag{3.7}$$

Using the displacement field definition, the deformation gradient is expressed as

$$\boldsymbol{F} = \boldsymbol{I} + \nabla_x \boldsymbol{u} \tag{3.8}$$

where $\boldsymbol{I}$ is the second order identity tensor. The use of equation 3.8 is convenient because allows the calculation of the deformation gradient once the displacements field is defined.

From the definitions above presented, and using infinitesimal geometric entities to establish the relation between reference and deformed configuration, we obtain

$$\begin{aligned} d\boldsymbol{x} &= \boldsymbol{F} d\boldsymbol{X} \\ d\boldsymbol{a} &= J\boldsymbol{F}^{-T} d\boldsymbol{A} \\ dv &= J dV \end{aligned} \tag{3.9}$$

where J, the Jacobian of the deformation, is the determinant of the deformation gradient.

$$J = \det(\boldsymbol{F}) \tag{3.10}$$

The determinant of the deformation gradient represents, locally, the volume after deformation per unit reference volume (or volume change ratio). If $J = 1$ the deformation is isochoric.

The isochoric/volumetric split of the deformation gradient is useful to solve some numerical issues such as the volumetric locking phenomena and is done as follows:

$$\boldsymbol{F} = \boldsymbol{F}_{iso}\boldsymbol{F}_v = \boldsymbol{F}_v\boldsymbol{F}_{iso} \tag{3.11}$$

where the volumetric and isochoric components of $\boldsymbol{F}$ are given respectively by

$$\boldsymbol{F}_v = (\det \boldsymbol{F})^{\frac{1}{3}} \boldsymbol{I} \tag{3.12}$$

and

$$\boldsymbol{F}_{iso} = (\det \boldsymbol{F})^{-\frac{1}{3}} \boldsymbol{I} \tag{3.13}$$

Whereas $\boldsymbol{F}_v$ corresponds to pure volumetric deformations, $\boldsymbol{F}_{iso}$ represents volume preserving deformations.

The F-bar deformation gradient [99,100] is obtained by replacing the regular volumetric part by the volumetric part calculated at the centroid of the element/knot span, $\boldsymbol{F}_0$, reading:

$$\bar{\boldsymbol{F}} = \boldsymbol{F}_{dev}(\boldsymbol{F}_0)_{vol} = \left(\frac{\det \boldsymbol{F}_0}{\det \boldsymbol{F}}\right)^{\frac{1}{3}} \boldsymbol{F} \tag{3.14}$$

The Polar Decomposition of the deformation gradient is useful to distinguish pure stretches from pure rotations and is decomposed as

$$\boldsymbol{F} = \boldsymbol{R}\boldsymbol{U} = \boldsymbol{V}\boldsymbol{R} \tag{3.15}$$

where $\boldsymbol{U}$ and $\boldsymbol{V}$ are unique, positive definite, symmetric tensors, termed, respectively right and left stretch tensors. $\boldsymbol{R}$ is the rotation tensor, unique proper orthogonal tensor[1].

The Right and Left stretch tensors can be rewritten as

$$\begin{aligned} \boldsymbol{U} &= \sqrt{\boldsymbol{C}} \\ \boldsymbol{V} &= \sqrt{\boldsymbol{B}} \end{aligned} \tag{3.16}$$

where $\boldsymbol{C}$ and $\boldsymbol{B}$ are the Right and Left Cauchy-Green strain tensors. By developing using the polar decomposition we arrive at

$$\begin{aligned} \boldsymbol{C} &= \boldsymbol{U}^2 = \boldsymbol{F}^T \boldsymbol{F} \\ \boldsymbol{B} &= \boldsymbol{V}^2 = \boldsymbol{F} \boldsymbol{F}^T \end{aligned} \tag{3.17}$$

The main assumption underlying the finite strain elasto-plasticity framework is that the deformation gradient can be decomposed in the product

$$\boldsymbol{F} = \boldsymbol{F}^e \boldsymbol{F}^p \tag{3.18}$$

where $\boldsymbol{F}^e$ $\boldsymbol{F}^p$ are the elastic and plastic deformations gradients, respectively.

Using this definition for the other kinematic quantities, the elastic right and left Cauchy-Green strain tensors are obtained by

$$\begin{aligned} \boldsymbol{C}^e &= (\boldsymbol{F}^p)^{-1} \boldsymbol{C} (\boldsymbol{F}^p)^{-T} \\ \boldsymbol{B}^e &= \boldsymbol{F} (\boldsymbol{C}^p)^{-1} (\boldsymbol{F})^T \end{aligned} \tag{3.19}$$

And the velocity gradient may be decomposed as

$$\boldsymbol{l} = \boldsymbol{l}^e + \boldsymbol{F}^e \boldsymbol{l}^p (\boldsymbol{F}^e)^{-1} \tag{3.20}$$

where we have defined

$$\boldsymbol{l}^e = \dot{\boldsymbol{F}}^e (\boldsymbol{F}^e)^{-1} \tag{3.21}$$

$$\boldsymbol{l}^p = \dot{\boldsymbol{F}}^p (\boldsymbol{F}^p)^{-1} \tag{3.22}$$

The strain tensor adopted to measure elastic deformations will be the logarithmic elastic strain tensor, which is expressed as

$$\boldsymbol{\varepsilon}^e = \ln \boldsymbol{V}^e = \frac{1}{2} \ln \boldsymbol{B}^e \tag{3.23}$$

where $\boldsymbol{B}^e = \boldsymbol{F}^e (\boldsymbol{F}^e)^T$

[1] A generic tensor $\boldsymbol{A}$ is orthogonal if $\boldsymbol{A}^T = \boldsymbol{A}^{-1}$. The determinant of a proper orthogonal tensor equals either +1 or -1.

3.1.3 Strain measures

After a given deformation, the material particles of a body occupy a different position in space. If the relative distance between the body particles remain the same, we are in a pure rotation case. On the other hand, if the relative distance between changes over deformation, the surrounding region is said to be strained. Straining is related to pure stretches, which in turn are characterised by the right and left Cauchy-Green strain tensors, $\boldsymbol{C}$ and $\boldsymbol{B}$, defined in the last subsection. Nevertheless, to quantify the relative distance change between two material points, that is, to characterize the straining, proper strain measures have to be defined.

There are numerous choices of strain tensors but, in practice, this choice is influenced by mathematical and physical convenience. An important class of strain measures is the so-called Lagrangian strain tensors, which are based on the right stretch tensor, given by

$$\boldsymbol{E}^{(m)} = \begin{cases} \frac{1}{m}(\boldsymbol{U}^m - I) & \text{if } m \neq 0 \\ \ln \boldsymbol{U} & \text{if } m = 0 \end{cases} \tag{3.24}$$

In a similar way, another important family of strain tensors can be defined by using the left stretch tensor $\boldsymbol{V}$. The Eulerian strain tensors are expressed as

$$\boldsymbol{e}^{(m)} = \begin{cases} \frac{1}{m}(\boldsymbol{V}^m - I) & \text{if } m \neq 0 \\ \ln \boldsymbol{V} & \text{if } m = 0 \end{cases} \tag{3.25}$$

Lagrangian and Eulerian strain tensors differs by the local rotation tensor $\boldsymbol{R}$ in the following way

$$\boldsymbol{e}^{(m)} = \boldsymbol{R}\boldsymbol{E}^{(m)}\boldsymbol{R}^T \tag{3.26}$$

In the following chapters we adopt the m=0 measure, that is, the evaluation of the logarithmic strain tensor (or Hencky strain tensor).

3.1.4 Velocity gradient

We define a gradient related to the velocity using the spatial field $\boldsymbol{l}$ expressed as

$$\boldsymbol{l} = \nabla_x \boldsymbol{v} \tag{3.27}$$

This velocity gradient may be expressed as function of the deformation gradient as

$$\boldsymbol{l} = \frac{\partial}{\partial t}\left(\frac{\partial \mathbb{X}}{\partial \boldsymbol{X}}\frac{\partial \boldsymbol{X}}{\partial \boldsymbol{x}}\right) = \dot{\boldsymbol{F}}\boldsymbol{F}^T \tag{3.28}$$

In its turn, the velocity gradient can be split into Stretch and Spin tensors respectively by

$$\begin{aligned} \boldsymbol{d} &= \tfrac{1}{2}\left(\boldsymbol{l}+\boldsymbol{l}^T\right) \\ \boldsymbol{w} &= \tfrac{1}{2}\left(\boldsymbol{l}-\boldsymbol{l}^T\right) \end{aligned} \tag{3.29}$$

where the tensor $\boldsymbol{d}$ is related with straining and is called the rate of deformation, and the tensor $\boldsymbol{l}$ is the spin tensor associated with rigid body velocity.

3.1.5 Infinitesimal deformations

Small or infinitesimal deformations are deformations with sufficiently small displacement gradient. The kinematics description can be simplified for this case.

Using the deformation gradient definition presented in equation 3.8, the Cauchy-Green strain tensors defined in 3.17 can be rewritten as

$$\begin{aligned} \boldsymbol{C} &= \boldsymbol{I}+\nabla_x\boldsymbol{u}+(\nabla_x\boldsymbol{u})^T+(\nabla_x\boldsymbol{u})^T\nabla_x\boldsymbol{u} \\ \boldsymbol{B} &= \boldsymbol{I}+\nabla_x\boldsymbol{u}+(\nabla_x\boldsymbol{u})^T+\nabla_x\boldsymbol{u}\,(\nabla_x\boldsymbol{u})^T \end{aligned} \tag{3.30}$$

If the displacement gradient $\nabla_X\boldsymbol{u}$ is sufficiently small, the second-order terms can be neglected, so we can made

$$\boldsymbol{C}\approx\boldsymbol{B}\approx\boldsymbol{I}+\nabla_x\boldsymbol{u}+(\nabla_X\boldsymbol{u})^T \tag{3.31}$$

which leads to a Lagrange strain tensor and its Eulerian counterpart defined in the following way [2]

$$\boldsymbol{E}^{(m)}\approx\boldsymbol{e}^{(m)}\approx\frac{1}{2}\left[\nabla_x\boldsymbol{u}+(\nabla_x\boldsymbol{u})^T\right] \tag{3.32}$$

This result motivates the definition of the infinitesimal strain tensor to measure strains under small deformations. Such tensor is defined as follows

$$\varepsilon=\frac{1}{2}\left[\nabla_x\boldsymbol{u}+(\nabla_x\boldsymbol{u})^T\right] \tag{3.33}$$

The infinitesimal strain tensor ε can also be split into a purely volumetric and a volume-preserving contribution. However, the split under small deformations is additive and reads

$$\varepsilon=\varepsilon_d+\varepsilon_v \tag{3.34}$$

where ε_v is the infinitesimal volumetric strain tensor and is the scalar invariant of ε, given by

$$\varepsilon_v=\operatorname{tr}\varepsilon \tag{3.35}$$

[2] error of second order for any m

For a volume preserving motion, $\varepsilon_v = 0$.

At its turn, the small strain elasto-plasticity framework is that the infinitesimal strain tensor is usually decomposed by the sum of the elastic and plastic component.

3.1.6 Stress measures

For each strain measure type it is possible to define a stress measure. The Cauchy or true stress tensor (or simply stress tensor) is given by

$$\boldsymbol{t} = \boldsymbol{\sigma}\boldsymbol{n} \tag{3.36}$$

where $\boldsymbol{t}$ is the surface traction and $\boldsymbol{n}$ is the associated normal vector. It states that the surface force $\boldsymbol{t}$ upon the normal $\boldsymbol{n}$ is linear. As a consequence, $\boldsymbol{\sigma}$ is symmetric.

Once again, the Cauchy stress tensor may be split in a deviatoric $\boldsymbol{s}$ and pressure p contributions as follows

$$\boldsymbol{\sigma} = \boldsymbol{s} + p\boldsymbol{I} \tag{3.37}$$

where

$$p = \frac{1}{3} tr[\boldsymbol{\sigma}] \tag{3.38}$$

In addiction, another important measure of stress is the Kirchhoff stress tensor, defined by

$$\boldsymbol{\tau} = J\boldsymbol{\sigma} \tag{3.39}$$

and is used widely in numerical algorithms in metal plasticity where there is no change in volume during plastic deformation.

Finally, the Piola-Kirchhoff stress tensors are indicated for finite strains applications and express the stress tensors relative to the reference configuration. This tensors are useful because does not expresses the stress relative to the present configuration as the Cauchy stress tensor do. For infinitesimal deformations and rotations, the Cauchy and Piola-Kirchhoff tensors are identical. The description of the stress, strain and deformation either in the reference or current configuration would make it easier to define constitutive models.

The 1st Piola-Kirchhoff stress tensor, $\boldsymbol{P}$ is one possible solution to this problem. It defines a family of tensors, which describe the configuration of the body in either the current or the reference state.

$$\boldsymbol{P} = \boldsymbol{\tau}\boldsymbol{F}^{-T} \tag{3.40}$$

The 2nd Piola-Kirchhoff stress tensor $\boldsymbol{S}$ relates forces in the current configuration to areas in the reference configuration and is given by

$$\boldsymbol{S} = \boldsymbol{F}^{-1}\boldsymbol{\tau}\boldsymbol{F}^{-T} \tag{3.41}$$

3.2 Conservation Principles

In the previous sections, the mathematical representation of phenomena such as deformation, motion and straining were made. However, they cannot be used for predictions if no relation among them is made. So, in this section, this concepts are related using some fundamental conservation principles, which are essential to formulate continuum mechanics problems. The detailed derivation of this principles may be found in the references [18, 101, 102].

3.2.1 Mass and Momentum Balance

The first principle regards the mass conservation and may be expressed as

$$\dot{\rho} + \rho \, \mathrm{div}_x \dot{\boldsymbol{u}} = \mathbf{0} \tag{3.42}$$

where ρ is the mass density at the deformed configuration.

The momentum balance, also referred as the strong form of the equilibrium equation, describes the equilibrium between internal and external forces in the body, and can be expressed as

$$\mathrm{div}_x \boldsymbol{\sigma} + \mathbf{b_f} = \rho \, \ddot{\boldsymbol{u}} \tag{3.43}$$

where $\boldsymbol{b_f}$ denotes the body force vector at the deformed configuration. These equation need the fulfil the following boundary conditions

$$\bar{\mathbf{t}} = \boldsymbol{\sigma}\mathbf{n} \tag{3.44}$$

where $\bar{\mathbf{t}}$ is the traction vector applied to the boundary of the body and $\mathbf{n}$ is the outward unit vector normal to the deformed boundary.

Equations 3.43 and 3.44 are formulated in the current body configuration. They may be expressed in the reference configuration of the body if we substitute the true stress tensor by first Piola-Kirchhoof stress tensor.

3.2.2 Thermodynamic Laws

The first law of thermodynamics postulates that the energy must be conserved and may be mathematically expressed as:

$$\rho \dot{e} = \boldsymbol{\sigma} : \boldsymbol{d} + \rho \, r - \mathrm{div}_x \boldsymbol{q} \tag{3.45}$$

where e represents the specific internal energy, $\boldsymbol{\sigma} : \boldsymbol{d}$ the specific stress power in current body configuration, r the density of heat production and $\boldsymbol{q}$ the heat flux. Throughout this thesis, only mechanical processes with constant temperature will be addressed, thus equation 3.45 reduces to

$$\rho \dot{e} = \boldsymbol{\sigma} : \boldsymbol{d} \tag{3.46}$$

The equation above states that the rate of internal energy per unit deformed volume must equal the stress power per unit deformed volume. As a consequence, the first law of thermodynamics may be rewritten in terms of the Kirchhoff stress tensor as follows

$$\bar{\rho} \dot{e} = \boldsymbol{\tau} : \boldsymbol{d} \tag{3.47}$$

where $\bar{\rho}$ is the reference mass density.

The Second Law of thermodynamics is associated with to the irreversibility of the entropy production, which may expressed as

$$\rho \mathrm{T} \dot{s} + \mathrm{div}_x \boldsymbol{q} - \rho\, r \geq 0 \tag{3.48}$$

where s is the entropy and T the temperature. For isothermal processes the second law of thermodynamics is given by

$$\rho \mathrm{T} \dot{s} \geq 0 \tag{3.49}$$

3.2.3 Clausius-Duhem Inequality

When the momentum balance law and the two laws of thermodynamics are combined we obtain the so-called Clausius-Duhem inequality

$$\boldsymbol{\sigma} : \boldsymbol{d} - \rho \dot{\psi} \geq 0 \tag{3.50}$$

where the left-hand side of 3.50 represents the dissipation per unit deformed volume and may be thought as an interesting inequality and a product relation to derive constitutive laws.

If we want to represent the above inequality in terms of dissipation per unit reference volume we get

$$\boldsymbol{\tau} : \boldsymbol{d} - \bar{\rho} \dot{\psi} \geq 0 \tag{3.51}$$

3.2.4 Helmholtz Free Energy

The Helmholtz free energy concept is defined as

$$\psi = e - Ts \tag{3.52}$$

and measures the useful work obtainable from a closed thermodynamic system at a constant temperature and volume. For such a system, the negative of the difference in the Helmholtz energy between two thermodynamical states is equal to the maximum amount of work extractable from the implicit thermodynamic process in which temperature and volume are held constant.

3.3 Constitutive Theory

The balance principles presented above are valid for any continuum body, regardless the material's body type. With the purpose of distinguish between different types of material, a constitutive model must be introduced. The use of internal variables to formulate constitutive models of dissipative materials is addressed. All dissipative constitutive models discussed along this work are based on the internal variable approach. A purely mechanical models are developed, neglecting the thermal effects on material properties.

Regarding the Thermodynamics with Internal Variables, at any instant t the thermodynamic state, defined by $\boldsymbol{\sigma}$, ψ and s at a given point $\boldsymbol{x}$, is determined by a finite number of state variables. As a consequence, the thermodynamic state only depends on the value of the state variables.

Once the state variables were chosen, according with the experimental observations of the mechanisms involved, the thermodynamics of irreversible processes requires the definition of two potentials:

- **State Potential**: to derive the state laws and define the variables associated with the internal variables ;
- **Dissipation Potential**: to derive the evolution laws of the state variables related with the dissipative mechanisms;
- **Yield Function**: to define the onset of plastic yielding;

3.3.1 The State Potential

For pure mechanical applications, the thermodynamical process at instant t is determined by the instantaneous values of the deformation gradient $\boldsymbol{F}$ and by a set of internal variables $\boldsymbol{\alpha}$[3] which are associated with the dissipative mechanisms:

$$\{\boldsymbol{F}, \boldsymbol{\alpha}\}$$

The choice of the set of internal variables is crucial if we want to kept successfully capturing all the stages of material behaviour.

[3] scalar, vectorial or tensorial

Usually, the specific Helmholtz free energy is taken as the state potential of the material and is given by a function of all state variables

$$\psi = \psi\left(\boldsymbol{F}, \boldsymbol{\alpha}\right) \tag{3.53}$$

and its rate of change is obtained making use of the chain rule as follows

$$\dot{\psi} = \frac{\partial \psi}{\partial \boldsymbol{F}} : \dot{\boldsymbol{F}} + \frac{\partial \psi}{\partial \alpha_k} : \dot{\alpha_k} \tag{3.54}$$

where summation over k is implied. Resorting both Clausius-Duhem inequality and the definition of specific stress power (per unit deformed volume) we obtain

$$\left(\boldsymbol{\sigma}\boldsymbol{F}^{-T} - \rho\frac{\partial \psi}{\partial \boldsymbol{F}}\right) : \dot{\boldsymbol{F}} - \rho\frac{\partial \psi}{\partial \alpha_k} : \dot{\alpha}_k \geq 0 \tag{3.55}$$

and in terms of power per unit reference volume we gets

$$\left(\boldsymbol{P}\boldsymbol{F}^{-T} - \bar{\rho}\frac{\partial \psi}{\partial \boldsymbol{F}}\right) : \dot{\boldsymbol{F}} - \bar{\rho}\frac{\partial \psi}{\partial \alpha_k} : \dot{\alpha}_k \geq 0 \tag{3.56}$$

The above equations must remain valid for any $\dot{\boldsymbol{F}}$. Thus, the constitutive equations for the first Piola-Kirchhoff, Cauchy, or Kirchhoff stress are given by

$$\boldsymbol{P} = \bar{\rho}\frac{\partial \psi}{\partial \boldsymbol{F}} \tag{3.57}$$

$$\boldsymbol{\sigma} = \frac{1}{J}\bar{\rho}\frac{\partial \psi}{\partial \boldsymbol{F}}\boldsymbol{F}^{T} \tag{3.58}$$

$$\boldsymbol{\tau} = \bar{\rho}\frac{\partial \psi}{\partial \boldsymbol{F}}\boldsymbol{F}^{T} \tag{3.59}$$

and they are all equivalent.

For each internal variable related to dissipative processes we define the conjugate thermodynamical force A_k as

$$A_k = \bar{\rho}\frac{\partial \psi}{\partial \boldsymbol{\alpha_k}} \tag{3.60}$$

which leads to a more compact form of the Clausius-Duhem inequality [4]

$$-\boldsymbol{A} * \dot{\boldsymbol{\alpha}} \geq 0 \tag{3.61}$$

The form of the function ψ is based on experimental observations. Usually is composed by the sum of the mechanisms involved, if there is no coupling between them.

[4] $*$ is the proper operator

3.3.2 The Dissipative Potential

The definition of the laws related to the dissipative processes are required in order to completely characterise the constitute model. We assume that the flux variables are a function of the state variables

$$\dot{\boldsymbol{\alpha}} = \phi(\boldsymbol{F}, \boldsymbol{\alpha}) \tag{3.62}$$

The possible form of the function ϕ is restricted by the Clausius-Duhem inequality. For the majority of the cases, an effective way to ensure the requirements of the Clausius-Duhem inequality consists in postulate a dissipation potential ϕ which is scalar-valued, convex, and respects the hypothesis of normal dissipativity.

For the most common materials the function ϕ is obtained using the associative flow rule, which means we will adopt the Von Mises Yield function to derive the evolution equations.

3.3.3 Constitutive Initial Value Problem

The generic constitutive problem using the internal variable approach consists in the following fundamental mechanical initial value problem: Given the initial values of the internal variables and the deformation gradient history: $\boldsymbol{\alpha}(t_0)$ and $\boldsymbol{F}(t)$, with $t \in [t_0, t_f]$. We need to find the functions $\boldsymbol{P}/t)$ and $\boldsymbol{\alpha}/t)$ such that

$$\begin{cases} \boldsymbol{P}(t) = \bar{\rho} \left. \frac{\partial \psi}{\partial \boldsymbol{F}} \right|_t \\ \dot{\boldsymbol{\alpha}}(t) = f(\boldsymbol{F}(t), \boldsymbol{\alpha}(t)) \end{cases} \tag{3.63}$$

are satisfied for every $t \in [t_0, t_f]$.

In the case of infinitesimal displacements, $\boldsymbol{P}$ and $\boldsymbol{F}$ are replaced by $\boldsymbol{\sigma}$ and ε.

The constitutive initial value problem allows the knowledge of the stress field history by the differentiation of the state potential. In its turn, the state potential is dependent on the internal variables evolution. To know the evolution laws a dissipative potential is created based on the dissipative mechanisms. Furthermore, an hardening criteria and the consistency condition need to be included into the model.

3.4 Concluding Remarks

Along this chapter the main entities and features of the CDM theory are presented. The F-Bar formulation is adopt and the equivalence beetwen small and finite strain models is described. The thermodynamics laws are applied in a pure mechanical sense and the basis of the constitutive theories based on thermodynamical state variables are outlined.

Chapter 4

Elasto-Plastic Models

This section starts with the description of the main physical mechanisms trough the deformation process. After that, the state and dissipative potentials are defined for each model. Finally, the Lemaitre damage-based constitutive theory for isotropic hardening is derived. For all formulations, the state and the evolution laws are derived.

4.1 Involved Mechanisms and Potential Functions

The Table 4.1 shows the considered mechanisms for the models, where R is the isotropic hardening variable, $\boldsymbol{C}^{kin}$ is a strain-like variable associated to kinematic hardening in line with reference [17], and D is the damage variable.

Table 4.1: State and Associated variables for each physical mechanism of deformation and damage.

Mechanisms		State Variables		Associated Variables
		observable	internal	
Elasticity	tensor	ε	or $\boldsymbol{B}$	$\boldsymbol{\sigma}$
Plasticity	tensor		ε^p or $\boldsymbol{B}^p$	$-\boldsymbol{\sigma}$
Isotropic Hardening	scalar		R	X
Kinematic Hardening	tensor		$\boldsymbol{C}^{kin}$	$\boldsymbol{K}$
Damage	scalar		D	-Y

At its turn, the Table 4.2 contains the form of the potential functions for all models.

Table 4.2: Potential functions form for the different models.

	State Potential	Dissipative Potential
Small Strain Isotropic Hardening	$\psi = \psi^e(\varepsilon^e) + \psi^{iso}(R)$	$\phi = \phi^p(\boldsymbol{\sigma})$
Finite Strain Isotropic Hardening	$\psi = \psi^e(\boldsymbol{B}^e) + \psi^{iso}(R)$	
Finite Strain Mixed Hardening	$\psi = \psi^e(\boldsymbol{B}^e) + \psi^{iso}(R) + \psi^{kin}\left(\boldsymbol{C}^{kin}\right)$	$\phi = \phi^p(\boldsymbol{\sigma}, \boldsymbol{\beta})$
Lemaitre Isotropic Hardening	$\psi = (1-D)\,\psi^e(\boldsymbol{B}^e) + \psi^{iso}(R)$	$\phi = \phi^p(\boldsymbol{\sigma}) + \phi^d(r,s)$

4.2 Elasticity

This physical mechanism only produces recoverable deformations, so doesn't have a dissipative potential associated. The previous loading history is of no importance.

For the small strain model a linear relation between stresses and strains was considered (Hooke's law). The elastic potential for this case is given by:

$$\frac{\psi^e(\varepsilon^e)}{\rho} = \frac{\lambda}{2}[\mathrm{tr}(\varepsilon^e)]^2 + \mu\,\mathrm{tr}(\varepsilon^e\varepsilon^e) \tag{4.1}$$

Regarding the finite strain models, Neo-Hookean (hyperelastic) law type was used. The respective elastic potential for this case is

$$\frac{\psi^e(\boldsymbol{B}^e)}{\rho} = \frac{\lambda}{4}(J_e - 1 - \log J_e) + \frac{\mu}{2}(\mathrm{tr}(\boldsymbol{B}^e) - 3 - \log J_e) \tag{4.2}$$

where $J_e = \det \boldsymbol{B}^e$, λ and μ are the Lamé parameters and ρ is the mass density.

4.3 Plasticity

The material is essentially elastic under the yield stress but, once this stress is attained the material is essentially plastic. The plastic behaviour is usually associated with deformations without volume change. To define the plastic regime we need a yield criterion, a normality hypothesis, and a consistency condition.

The yield function defines the limit at which material becomes plastic, the flow rule describe the strain-stress relation at plastic regime, and the consistency condition prevents stresses from exceeding the yield limit. Based on experimental observations, the metal is described as incompressible, insensitive to hydrostatic pressure, and follow the associated flow rules.

In other words, the definition of an dissipative potential requires the use of an yield function, which in this case is the von Mises criteria [1]. Once the dissipative potential is characterised, the yield criterion is given by $\phi = 0$, and a flow rule and a hardening law are obtained. So, this dissipative potential will allow to know the evolution of the hardening

[1] The criterion is based on that the yielding occur when the distortion elastic energy reaches an critical value in a tensile test.

parameters. These hardening parameters are introduced in the associated state potential and the stress field is updated [3].

4.3.1 Isotropic Hardening

Regarding the isotropic hardening, the isotropic plastic part of the free energy reads:

$$\frac{\psi^{iso}(R)}{\rho} = R_\infty \left[R + \frac{1}{\delta} e^{-\delta R} \right] \tag{4.3}$$

where R_∞ represents the saturation value of the isotropic hardening while δ is the saturation exponent [2].

In order to determine the evolution equations of the constitutive models, the dissipative potentials have to be specified. For the plastic part, assuming the strain equivalence principle, the von Mises yield function may be adopted in the following way

$$\phi^p = \sqrt{\frac{3}{2} \boldsymbol{\tau} : \boldsymbol{\tau}} - \tau(R) \tag{4.4}$$

where $\tau(R)$ is the yield function that results from the uniaxial tensile test results from a material of yield stress τ_Y, and is given by

$$\tau(R) = \tau_Y + K(\varepsilon - \varepsilon^e) + R_\infty \left[1 - e^{-\delta(\varepsilon - \varepsilon^e)} \right] \tag{4.5}$$

For small strains problems the Kirchhoff $\boldsymbol{\tau}$ stress tensor may be replaced by the Cauchy stress tensor $\boldsymbol{\sigma}$.

4.3.2 Mixed Hardening

The kinematic plastic part of the free energy is defined as follows

$$\frac{\psi^{kin}\left(\boldsymbol{C}^{kin}\right)}{\rho} = \frac{1}{2} H_k \left(tr\left(\boldsymbol{C}^{kin}\right) - 3 \right) \tag{4.6}$$

where H_k represents the kinematic hardening modulus.

To include the kinematic hardening effect in the dissipative process, the Kirchhoff stress tensor in the dissipation potential has to be replaced by the difference:

$$\phi^p = \sqrt{\frac{3}{2} (\boldsymbol{\tau} - \boldsymbol{\beta}) : (\boldsymbol{\tau} - \boldsymbol{\beta})} - \tau(R) \tag{4.7}$$

where $\boldsymbol{\beta}$ is the back-stress tensor that will be defined in section 4.4.3. The above equation corresponds to a Prager type of kinematic hardening function. Nevertheless, unrealistic stress oscillations in the numerical solutions are reported when this law is used

[2] Usually obtained by a minimum square approximation from a uniaxial tensile test.

in a finite strain context. To overcome this problem, the plastic dissipative potential may be enhanced as follows:

$$\phi^p = \sqrt{\frac{3}{2}(\boldsymbol{\tau}-\boldsymbol{\beta}):(\boldsymbol{\tau}-\boldsymbol{\beta})} - \tau(R) - \frac{1}{2}b_{sat}\boldsymbol{\beta}:\boldsymbol{\beta} \tag{4.8}$$

From equation 4.8, an Armstrong-Frederick type of kinematic hardening rule is retrieved [103]. The parameter b_{sat} is related to the saturation of the kinematic hardening, although its physical interpretation is not obvious. Setting $b_{sat} = 0$, the Prager law is recovered.

4.4 Damage

4.4.1 Effective Stress Concept

Damage may be interpreted at the microscale as the breaking of atomic bonds and plastic enlargement of micro cavities [6]. However, the quantification of the micro-defects at the mesoscale level, may be taken in account in a averaging sense. The damage variable $D_{\hat{n}}$ is defined as

$$D_{\hat{n}} = \frac{\partial S_D}{\partial S} \tag{4.9}$$

where ∂S is the area of the intersection of the plane with the representative volume element (RVE), with normal $\hat{n}$, and ∂S_D is the area that effectively intersects cavities or micro-cracks.

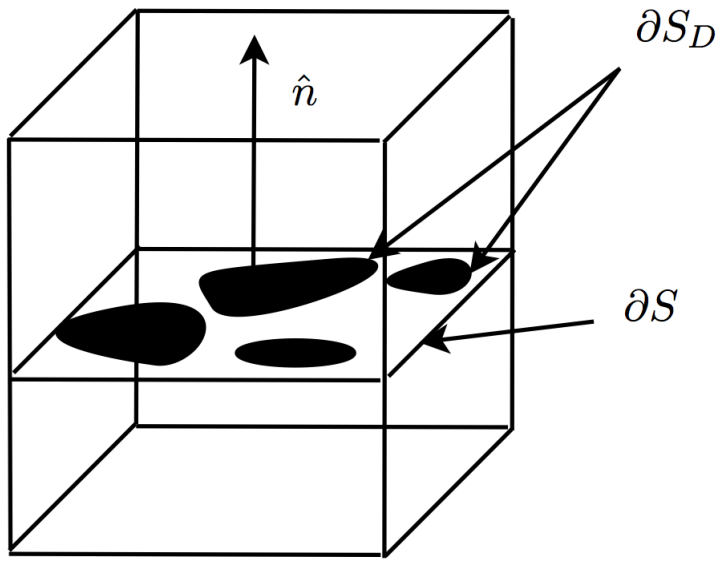

Figure 4.1: Representative Volume Element [2].

The RVE size of a certain material is defined in such a way that all the properties are represented by homogenised variables and for metals is around 0.1 mm^3 [6]. In addiction, when only ductile damage is considered, D is isotropic and represented by a scalar variable, ranging from 0 to 1(undamaged to fully damage material respectively). However, a second or fourth order tensor representation may be adopted for general applications [6].

In the previous sections the strain and stress measures were introduced to be used in the constitutive equations that characterize a given virgin material, however, in the presence of damage (any manufactured material) the resistant area is smaller and the effective Cauchy stress tensor may be introduced as:

$$\bar{\boldsymbol{\sigma}} = \frac{\boldsymbol{\sigma}}{1-D} \tag{4.10}$$

where $\boldsymbol{\sigma}$ is the Cauchy stress tensor for undamaged material. From this definition it follows the strain equivalence principle, which states that a damaged material is governed by the constitutive laws of the plain material, replacing the true stress by the effective stress.

4.4.2 Lemaitre model

As a consequence of the effective stress concept the dissipation potential due to isotropic hardening turns into

$$\phi^p = \frac{1}{1-D}\sqrt{\frac{3}{2}\boldsymbol{\tau} : \boldsymbol{\tau}} - \tau(R) \tag{4.11}$$

From the micro-mechanical point of view, the damage dissipative process is associated to the irreversible rupture of atomic bonds, while plastic dissipation is a consequence of the movement and accumulation of dislocations, which cause irreversible deformations. Therefore, the effects of all three mechanisms may be considered in a decoupled way, defining as:

$$\phi = \phi^p + \phi^d \tag{4.12}$$

where ϕ^p and ϕ^d are the energy potentials associated with isotropic plasticity and damage, respectively. For the damage dissipation potential, the following function based in the work of Lemaitre [6] will be employed:

$$\phi^d = \frac{r}{(s+1)(1-D)}\left[\frac{-Y}{r}\right]^{s+1} \tag{4.13}$$

where r and s are scalar material parameters associated with damage evolution.

4.4.3 Associated Variables

For the free energy, the following associated variables, depends on the model, may be defined.

The constitute relation is given by

$$\boldsymbol{\tau} = 2\rho \boldsymbol{B}^e \frac{\partial \psi}{\partial \boldsymbol{B}^e} \tag{4.14}$$

And the associate thermodynamical forces are obtained as

$$X = \rho \frac{\partial \psi}{\partial R} \tag{4.15}$$

$$Y = -\rho \frac{\partial \psi}{\partial D} \tag{4.16}$$

$$\boldsymbol{K} = \rho \frac{\partial \psi}{\partial \boldsymbol{C}^{kin}} \tag{4.17}$$

where X are the thermodynamical forces conjugated with isotropic hardening and Y is the damage energy release rate. Regarding the mixed model, the tensor $\boldsymbol{K}$ is a stress-like variable which will lead to the definition of the back-stress tensor, as follows:

$$\boldsymbol{b} = \boldsymbol{C}^{kin}\boldsymbol{K} = H_k \boldsymbol{C}^{kin\,dev} \tag{4.18}$$

Using equation 4.6, the back-stress becomes

$$\boldsymbol{b} = H_k \boldsymbol{C}^{kindev} \tag{4.19}$$

where $\boldsymbol{C}^{kindev}$ is the deviatoric part of $\boldsymbol{C}^{kin}$, which means that the back stress is a deviatoric stress. It may be written in the spatial configuration as:

$$\boldsymbol{\beta} = \boldsymbol{R}^e \, \boldsymbol{b} \, \boldsymbol{R}^{e^T} \tag{4.20}$$

where $\boldsymbol{R}^e$ is the elastic rotation tensor obtained from the polar decomposition of the elastic deformation gradient.

4.4.4 Evolution Equations

The function $\phi + \tau(R)$ is the yield surface. In theory, if the yield surface is exceeded we get plastic deformation. However, because of the plastic flow, the yield surface is expanded (isotropic hardening) and/or translated (kinematic hardening) in manner that the stress state stays on the yield surface. The yield function can take a several analytical expressions whose geometrical representation have distinct domains. Usually, the yield surface is represented on Westergaard space, where the three principal directions are coincident with the referential axes [104,105]. Figure 4.2 shows 3 different behaviours for a specimen

subjected to a traction-compression scenario and Figure 4.3 shows the initial and final (dashed) configurations of the yield surface in the Westergaard space.

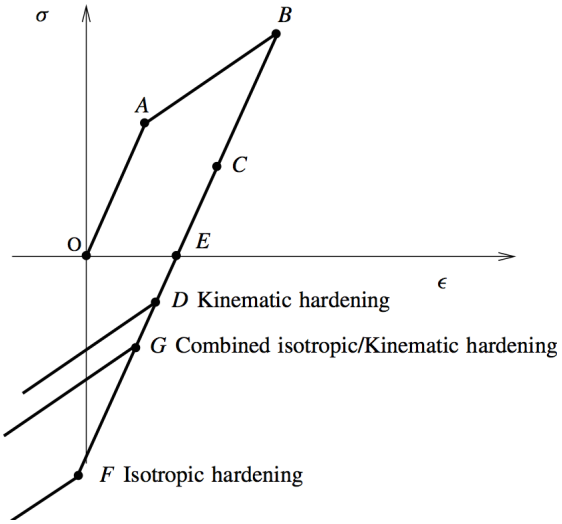

Figure 4.2: Traction-compression scenario for 3 hardening types [3].

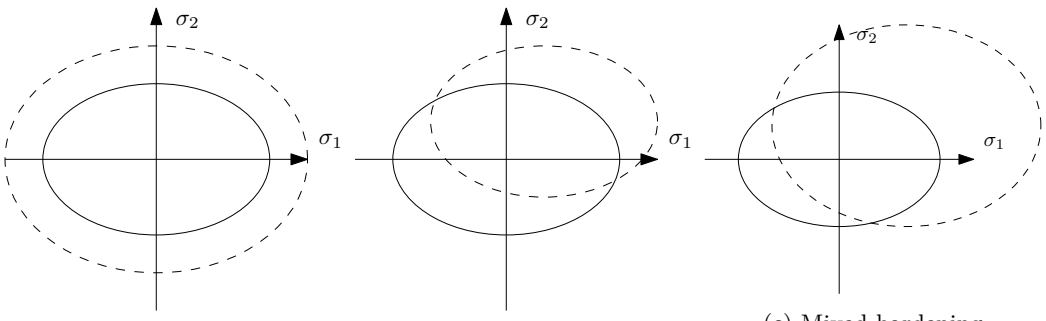

(a) Isotropic hardening (b) Kinematic hardening (c) Mixed hardening

Figure 4.3: Initial and final configurations of the Yield surface.

In other words, when the current stress state of the material lies within the yield surface, the material behaves purely elastically but, once load path intersects the yield surface the stress state must stay on the yield surface. Although this surface can move and change shape as the hardening parameters changes.

Briefly, the yield function ϕ returns the following cases [104, 106]:

- If $d\phi < 0$, indicates that exist a unloading situation. The stress state is located at the interior of yield surface and the material is at elastic regime.
- If $d\phi = 0$, the stress state is at yield surface;
- If $d\phi > 0$, the stress state remain at yield surface but the surface geometry changes if the material have hardening.

Finally, making use of the normality rule it is possible to determine the evolution equations.

The associated flow rule is given by

$$L_v \boldsymbol{B}^e = -2\dot{\gamma}\frac{\partial \phi}{\partial \boldsymbol{\tau}}\boldsymbol{B}^e \tag{4.21}$$

or, for small strain theories, by

$$\varepsilon^p = \dot{\gamma}\frac{\partial \phi}{\partial \boldsymbol{\sigma}} \tag{4.22}$$

The vectors $\frac{\partial \phi}{\partial \boldsymbol{\tau}}$ and $\frac{\partial \phi}{\partial \boldsymbol{\sigma}}$ are normal to the yield surface. As a consequence, the plastic strain increment vector is also normal to the yield surface, which ensures a unique solution (normality hypothesis) [107].

In its turn, the hardening law is performed as

$$\dot{R} = -\dot{\gamma}\frac{\partial \phi}{\partial X} = \dot{\gamma} \tag{4.23}$$

and the damage evolution is attained as

$$\dot{D} = \dot{\gamma}\frac{\partial \phi}{\partial (-Y)} = \dot{\gamma}\frac{1}{1-D}\left(\frac{-Y}{r}\right)^s \tag{4.24}$$

where L_v represents the spatial velocity Lie derivative[3] and γ is the plastic multiplier. In the mixed hardening model, the back-stress is obtained from the tensor $\boldsymbol{C}^{kin}$, whose evolution equation is of the same type as the evolution equation for the deformation gradient, as follows:

$$\dot{\boldsymbol{F}}^p = \dot{\gamma}\frac{\partial \phi}{\partial \boldsymbol{\tau}}\boldsymbol{F}^p \tag{4.25}$$

$$\dot{\boldsymbol{C}}^{kin} = \dot{\gamma}\frac{\partial \phi}{\partial \beta}\boldsymbol{C}^{kin} \tag{4.26}$$

4.4.5 Consistency Condition

The requirement for the load point to remain on the yield surface during plastic deformation is called the consistency condition [108]. This condition enables the determination of plastic multiplier γ . In other words, the consistency condition is a mathematical expression of the requirement that the stress state stay on the yield surface as long as loading continues, even though the yield surface itself will be moving and changing shape due to hardening.

[3] derivative of tensor $\boldsymbol{B}^e$ with respect to the velocity vector

For the small strains models the Kuhn-Tucker conditions are

$$\begin{aligned} &\dot{\gamma} \geq 0 \\ &\phi \leq 0 \\ &\dot{\gamma}\dot{\phi} = 0 \\ &\text{for all } \vee \boldsymbol{x} \in V \end{aligned} \tag{4.27}$$

and for finite strains we get

$$\begin{aligned} &\dot{\gamma}(\boldsymbol{x}) \geq 0 \\ &\boldsymbol{F}^p \leq 0 \\ &\dot{\gamma}(\boldsymbol{x})\dot{\boldsymbol{F}}^p = 0 \\ &\text{for all } \vee \boldsymbol{x} \in V \end{aligned} \tag{4.28}$$

which both must hold globally in the domain, V.

4.5 Concluding Remarks

The mechanisms involved trough the deformation process are evaluated in a simple manner. The state and dissipative potentials functions are derived. The thermodynamical forces obtained from the free energy are used to establish the evolution equations, which in its turn, will set the displacement field.

Chapter 5

FE Discretisation and Computational Implementation

In order to formulate nonlinear isogeometric elements symbolically in a general and simple way, the mathematical formulation presented on chapters 2, 3 and 4 simultaneously with the discretization processes is evaluated at the highest abstract level possible. Appropriate problem descriptions for the fully implicit analysis of non-linear, path-dependent problems and a simplified symbolic input for the generation of isogeometric elasto-plastic elements are presented on this chapter. Previous developed elasto-plastic finite element models were included into an hyperelastic isogeometric model using the AceGen and AceFEM systems.

5.1 FE discretisation

5.1.1 Virtual Work Principle

Recalling the momentum equilibrium for the static case and neglecting the body forces we get

$$\text{div}_x \boldsymbol{\sigma} = \mathbf{0} \tag{5.1}$$

and integrating over the domain $\mathbb{B}$ for any virtual displacement $\boldsymbol{\eta}$ results in

$$\int_{\mathbb{B}(\Omega)} (\text{div}_x \boldsymbol{\sigma})^T \boldsymbol{\eta} dv = 0 \tag{5.2}$$

Using the divergence theorem results in

$$\int_{\mathbb{B}(\Omega)} \boldsymbol{\sigma} : \nabla_x \boldsymbol{\eta} dv - \int_{\mathbb{B}(\partial\Omega)} (\boldsymbol{\sigma} \cdot \boldsymbol{n})^T \boldsymbol{\eta} da = 0 \tag{5.3}$$

fulfilled by the boundary condition

$$\bar{\boldsymbol{t}} = \boldsymbol{\sigma}\boldsymbol{n} \tag{5.4}$$

Replacing this relation in equation 5.3, the weak form of the equilibrium equation is obtained:

$$\int_{\mathbb{B}(\Omega)} \boldsymbol{\sigma} : \nabla_x \boldsymbol{\eta} dv - \int_{\mathbb{B}(\partial\Omega)} \bar{\boldsymbol{t}}^T \boldsymbol{\eta} da = 0 \tag{5.5}$$

And can be seen as the equilibrium between internal and external works for any virtual displacement vector respecting the boundary and initial conditions of the problem.

$$W_{\text{int}} - W_{ext} = 0 \tag{5.6}$$

$$W_{ext} = \int_{\mathbb{B}(\partial\Omega)} \bar{\boldsymbol{t}}^T \boldsymbol{\eta} da = \int_{\partial\Omega} \bar{\boldsymbol{t}}_0^T \boldsymbol{\eta} dA \tag{5.7}$$

$$W_{\text{int}} = \int_{\mathbb{B}(\Omega)} \boldsymbol{\sigma} : \nabla_x \boldsymbol{\eta} dv = \int_{\Omega} \boldsymbol{P} : \nabla_X \boldsymbol{\eta} dV \tag{5.8}$$

5.1.2 Displacements interpolation

In this work, a displacement-based isogeometric elements is used. Thus, the interpolated field variables are the displacements, which within a given element e assume the form:

$$\boldsymbol{u}(\boldsymbol{x}) = \sum_{i=1}^{nknot} {R_i}^{(e)}(\boldsymbol{x})\, \boldsymbol{u}_i \tag{5.9}$$

where ${R_i}^{(e)}$ is the shape function of the knot i and $nknot$ is the number of knots of the knot span (or element). If the entire domain is composed by $nctrl$ control points the global displacement vector in a problem of dimension $ndim$ is given by

$$\boldsymbol{u} = \left[{u_1}^1, \cdots, {u^1}_{ndim}, \cdots, {u_1}^{nctrl}, \cdots, {u^{nctrl}}_{ndim} \right] \tag{5.10}$$

and $\boldsymbol{R}^g$ is the global interpolation matrix, defined as:

$$\boldsymbol{R}^g = \left[\begin{array}{cccc} \text{diag}\left[{R_1}^g(\boldsymbol{x})\right] & \text{diag}\left[{R_2}^g(\boldsymbol{x})\right] & \cdots & \text{diag}\left[{R_{nctrl}}^g(\boldsymbol{x})\right] \end{array} \right] \tag{5.11}$$

where each $\text{diag}\left[{R_i}^g(\boldsymbol{x})\right]$ is a $ndim \times ndim$ diagonal matrix with the shape function value for knot i

The displacement and virtual displacements fields are now expressed in a condensed form as

$$\begin{aligned} \boldsymbol{u}(\boldsymbol{x}) &= \boldsymbol{R}^g \boldsymbol{u} \\ \boldsymbol{\eta}(\boldsymbol{x}) &= \boldsymbol{R}^g \boldsymbol{\eta} \end{aligned} \tag{5.12}$$

Note that the discretised form of the equilibrium equation is identical to the classical finite element method. However, the construction process of the shape functions and also the application of the isoparametric concept to get the values of the shape functions in the physical space differs from the classical FEM, was explained in section 2.4.2.

5.1.3 Computational Implementation

The process start from the Helmholtz free energy ψ, and the derivation of the element equations are obtained directly as a gradient of the free energy. This gradients are obtained using the reverse mode of automatic differentiation [109]. So, this process represents essentially the coding of a different element kinematics and/or a different material model only at the element level, which suggests that a large number of operations related to FEM programming could be automated [2]. The only free parameters of the formulation are the strain energy function, the yield condition, the evolution equations and the discretisation of the domain and displacements [2].

The AceGen System [96] employs the Simultaneous Stochastic Simplification of Numerical Code approach [110,111], which combines an automatic differentiation technique with the simultaneous optimisation of symbolic expressions, allowing the automatic generation of efficient numerical methods codes.

In this model, the equilibrium equation is, in general, non-linear and the Cauchy stress is dependent of the strains history. As a consequence it is essential the definition of a suitable pseudo-time discretisation between the time increments $[t_n, t_{n+1}]$ in order to integrate a fully implicit scheme.

The following function,

$$\boldsymbol{\sigma} = \hat{\boldsymbol{\sigma}}(\boldsymbol{F}_{n+1}, \boldsymbol{\alpha}_n) \tag{5.13}$$

is associated with an integration algorithm that delivers the stress state for a given deformation gradient,$\boldsymbol{F}_{n+1}$, and for a given set of internal variables, $\boldsymbol{\alpha}_n$, which are assumed to be constant within the one increment.

The Newton-Raphson algorithm is attractive for the solution of this type of problems due to its robustness and quadratic rates of asymptotic convergence. During a solution procedure in which equilibrium is not yet satisfied, there is a residual R between the internal work (or forces) and the external work (or forces) [2]. In our case, the applied

traction is independent of the deformation, and the individual element contribution to the residual may be defined as:

$$\boldsymbol{R}_e\left(\boldsymbol{u}_{n+1}\right) = \boldsymbol{R}_{en+1} = \int_{\Omega_e} \boldsymbol{P}_{n+1} \frac{\partial \boldsymbol{F}_{n+1}}{\partial \boldsymbol{u}_{en+1}} d\mathbb{B} \tag{5.14}$$

where Ω_e is the domain of the element. Following the general procedures of the Newton method, a system of equations of the the form

$$\boldsymbol{R}_{n+1} = 0 \tag{5.15}$$

is obtained if convergence occurred.

The global residual depends on the previous and current time step global displacement vectors, that is

$$\boldsymbol{R}_{n+1} = \boldsymbol{R}_{n+1}(\boldsymbol{u}_{n+1}, \boldsymbol{u}_n) \tag{5.16}$$

and therefore, the (k^{th}) iteration step may be written as

$$\boldsymbol{K}^k_{Tn+1} \Delta \boldsymbol{u}^k{}_n + \boldsymbol{R}^k{}_{n+1} = 0 \tag{5.17}$$

where K_T is the global tangent stiffness matrix given by

$$\boldsymbol{K}^k{}_{Tn+1} = \frac{\partial \boldsymbol{R}^k{}_{n+1}}{\partial \boldsymbol{u}^k{}_{n+1}} \tag{5.18}$$

Finally, the displacements are updated as follows:

$$\boldsymbol{u}_{n+1}{}^{k+1} = \boldsymbol{u}^k{}_{n+1} + \Delta \boldsymbol{u}^k{}_{n+1} \tag{5.19}$$

The implementation of a FEM code may be quite complicated and time consuming when dealing with non-linear material models. In general, the discretisation and linearisation procedures described in the previous sections have to be performed prior to the actual code writing. The complexity of the required calculations increases the probability of error and, consequently, inefficient codes may result [2].

After a brief description of the AceGen and AceFEM systems, it will be now illustrated how these tools can be used to generate a FEM code. Firstly, AceGen systems are oriented to generate code at the single element level. The application of automatic differentiation procedures to a complete FEM environment may become inefficient especially when fully implicit Newton-type procedures are used to solve highly non-linear problems. However, this problem is easily overcome by generating routines to evaluate specific quantities, at the individual element level, such as the consistent stiffness tangent matrix, the element

force vector, the stress or strain tensors. Later, different elements may be combined for the analysis step in AceFEM.

Writing a code using a symbolical formulation often differs from the traditional computational mechanics approach because the intermediate quantities (variables) do not appear explicitly in automatically generated codes. The final code shows the formulation at the highest abstract level possible in a clear way. This type of formulation is more compressed resulting in fewer possibilities of error. Moreover, derivatives obtained automatically from the symbolic description are exact, leading to quadratically convergent Newton-type of iterative schemes [2].

Having in mind the above considerations, there are three main steps that should be considered in the generation of a finite element using AceGen, as follows [112]:

1. **Initialization** - the element characteristics are defined in a global set of constants, such as the element topology, the number of history variables, the material parameters, the finite element environment, and others. The kinematics and the constitutive equations are also developed.

2. **Tangent and Residual** - Definition of the stiffness tangent matrix and element force vector for the discretisation and material model defined in the Initialisation step. It should be noticed that the element contribution to the global force vector, $\boldsymbol{R}$, considering the global set of unknowns, $\boldsymbol{p}$, is automatically derived using the relation:

$$\boldsymbol{R}_{en+1} = \int_{\Omega_e} \boldsymbol{P}_{n+1} \frac{\partial \boldsymbol{F}_{n+1}}{\partial \boldsymbol{p}_{en+1}} d\mathbb{B} \tag{5.20}$$

   The contribution to the global stiffness matrix, K is also automatically calculated as

$$\boldsymbol{K}_{Ten+1} = \frac{\partial \boldsymbol{R}_{en+1}}{\partial \boldsymbol{p}_{en+1}} \tag{5.21}$$

   The constitutive equations are only developed once, before the code writing, saving time and reducing the probability of error.

3. **Post-processing** - extrapolation of the strains and stresses and other relevant fields, from the Gauss points to the nodes followed by adequate graphics treatments of the results.

In order to create the elasto-plastic models based on an isogeometric approach we proceeded in the following way:

- First, the study of the AceGen symbolic code, related to the already developed models presented on the AceFEM library were made: An elastoplastic finite element model and an hyperelastic isogeometric model;

- After that, the integration of the elastoplastic constitutive equations into the isogeometric model were performed;
- New data arrays were created to include the elastoplastic state variables.
- Finally, the data arrays were exported to the control points. These arrays are used in each iteration of the Newton-Raphson method performed by AceFEM routines;

5.2 Concluding Remarks

The virtual work principle is applied to the momentum balance equation followed by the discretization applied to the displacements field. The computational process is summarised and some features off the AceGen system and code developing notes are itemised.

Chapter 6

Numerical Results

In this chapter, the isogeometric models are evaluated from the numerical point of view. The goal is the validation of the constructed IGA models in ductile materials such as some alloy steels structures, under different load paths. The formulations proposed in the previous chapters are implemented in a finite element code featuring the following aspects:

- Implicit Iterative Solution;
- 3D Hexahedral Finite Element topology with 8 nodes/knots points for FE models and for first order NURBS functions. For the second order NURBS functions the topology of the element is defined with 27 knots;
- Selective-Reduced numerical integration under an F-bar formulation. That is, 1 Gauss Point for the volumetric stress and the typical Gauss Quadrature rule for the deviatoric stress. More specifically, the deviatoric stress integration for the FEM and first order NURBS models were made using 8 Gauss Points [1]. For the second order NURBS functions, the integration rule were applied using 27 Gauss Points.
- Small and finite strains models;
- Isotropic and mixed isotropic-kinematic hardening models;
- Lemaitre model with isotropic hardening under a local formulation;

The proposed formulations will be evaluated in different aspects using 4 distinct geometries: a solid block subjected to a compression pressure; a thick cylindrical shell subjected to a line pressure; a clamped bar with progressively reduced section subjected to a vertical cyclic load on the top mesh and a plane stress specimen subjected to a tensile force.

[1] Unless in the cases where is explicitly specified

In the case of the block example, the effects of mesh size, number of integration Gauss points, and the basis functions order are studied over the isotropic hardening models. Also, the differences between small and finite strains models are evidentiated ranging the compression pressure value. After that, the thick cylindrical results are compared with the work done in [113].

Next, the mixed isotropic-kinematic hardening models are studied over the clamped bar example. The bar is subjected to 5 load cycles. Finally, for the case of the plane stress specimen, the analysis is devoted to notice the damage effect over the structure and to compare with the no damaged models. In this case, the specimen is subjected to traction load.

In order to describe the solutions of the models in a simplified way, the formulations are referenced as is the Table 6.1.

Table 6.1: Models references. FEM or IGA basis.

Description	Model
Small Strain Isotropic Hardening	SS-ISO-FEM/IGA
Finite Strain Isotropic Hardening	FS-ISO-FEM/IGA
Finite Strain Mixed Hardening	FS-ISOKIN-FEM/IGA
Lemaitre Isotropic Hardening	FS-ISODAM-FEM/IGA

6.1 Compression of a Block

The block represented in Figure 6.1 is subjected to a compression pressure at its center. For symmetry reasons only a quarter of the block is represented. Regarding the boundary conditions, the upper face points only move in vertical direction and there are no vertical displacements on the bottom surface. Also, the mechanical properties are presented in Table 6.2, where the block was considered with linear isotropic hardening. The results were performed in order to test the IGA isotropic hardening model by comparison with the FEM model, measuring the vertical displacement of the center point for different mesh sizes.

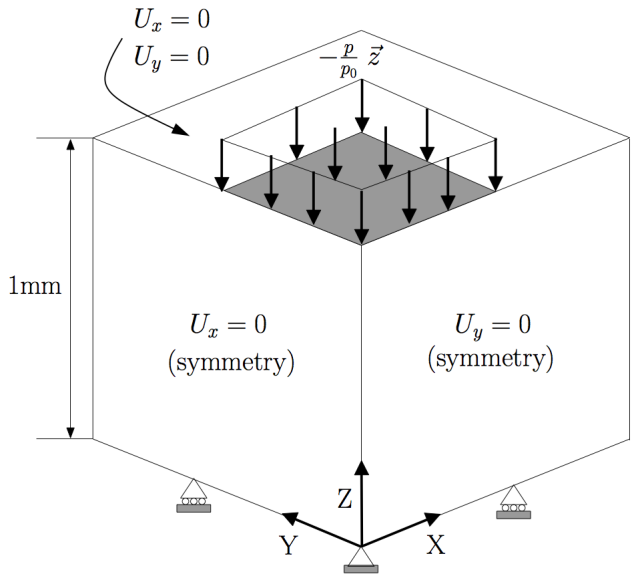

Figure 6.1: Compression test: geometry, boundary conditions and loading.

Table 6.2: Compression test block mechanical properties.

Young Modulus	E =210000 MPa
Poisson's ratio	v =0.3
Yield Stress	τ_Y=150 MPa
Isotropic Hardening Modulus	K =120 MPa

In Figure 6.2, we evaluate the mesh dependence of the finite strain model. Setting the pressure as 450 MPa we can see that isogeometric model converge to the FE solution (FS-ISO-FEM) as we approach to the finest meshes. In general, all isogeometric models have a stiffer response. The first order basis IGA models (FS-ISO-IGA) have the same behaviour, regarding the number of Gauss points used. In addiction, using second degree NURBS (FS-ISO-IGA-2p) the results are slightly better for coarse meshes. However, the second order NURBS models trend to get a stiffer respond comparing with other IGA models.

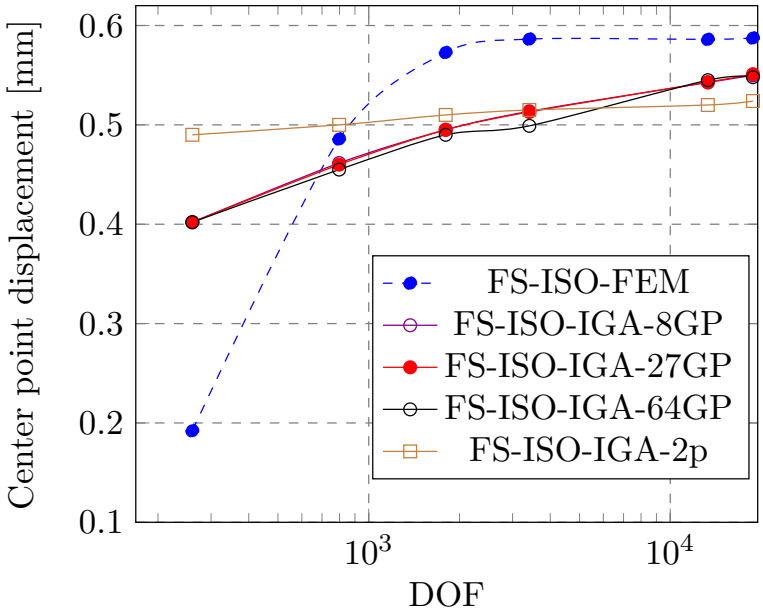

Figure 6.2: Center point vertical displacement for finite strain isotropic hardening models using different mesh sizes.

Ranging the pressure value from 300 to 450 MPa with the finest meshes from the last evaluation we can now evaluate the differences between small and finite strain models. As we see in Figure 6.3, the vertical displacement of the center point diverges as the pressure value increases.

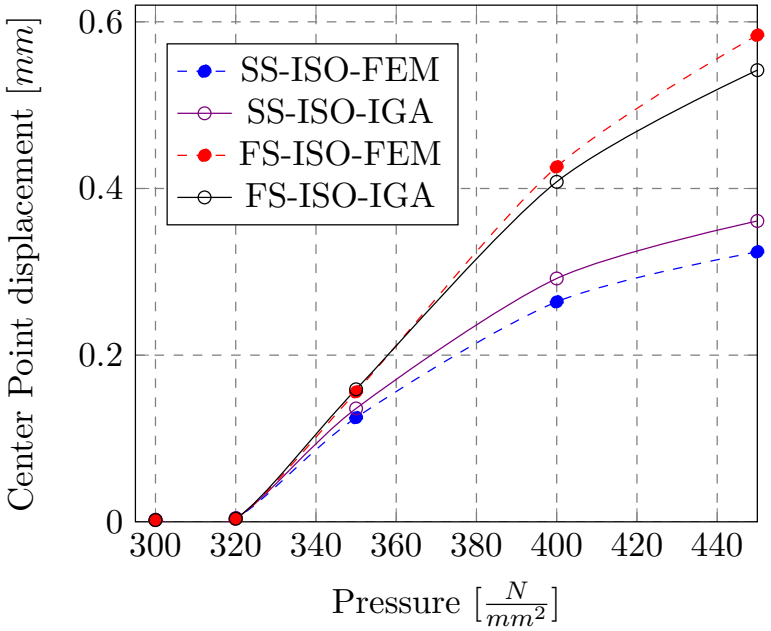

Figure 6.3: Center point vertical displacement for different pressure values. Comparison between small and finite strain isotropic hardening models.

Regarding the results, since the NURBS shape functions of the first degree are identical

as the linear Lagrange polynomials it was expected to get more approximate solutions comparing with FE models. This deviation may be related to the F-bar implementation.

Besides that, the solutions shows the convergence of IGA models. Regarding the F-bar formulation, further investigations need to be applied in order to reach fully IGA developed models. Which in this case is the performance of the F-bar formulation by patch rather than knot span.

Finally, Figure 6.4 contains the accumulated plastic deformation field (or effective plastic strain field) and the final deformed configuration for FS-ISO-FEM and FS-ISO-IGA models with 18810 DOF at its maximum pressure magnitude: 450 MPa.

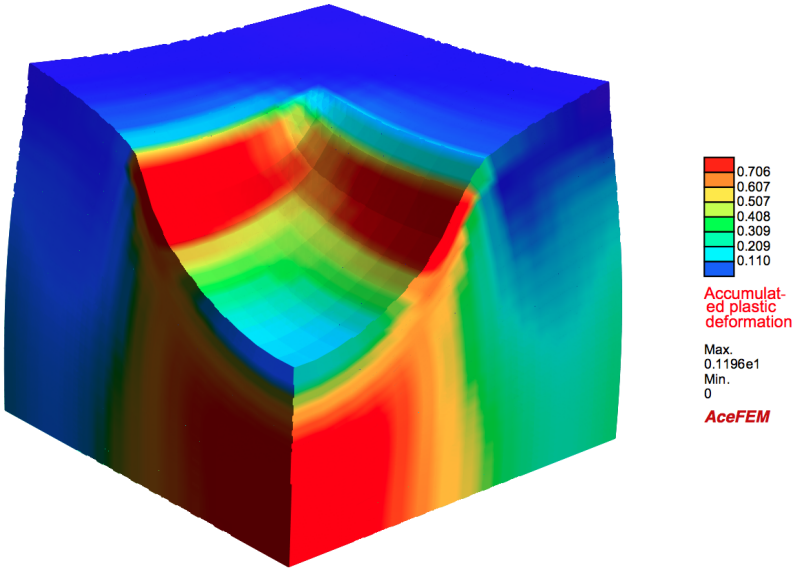

(a) FS-ISO-IGA: isotropic hardening

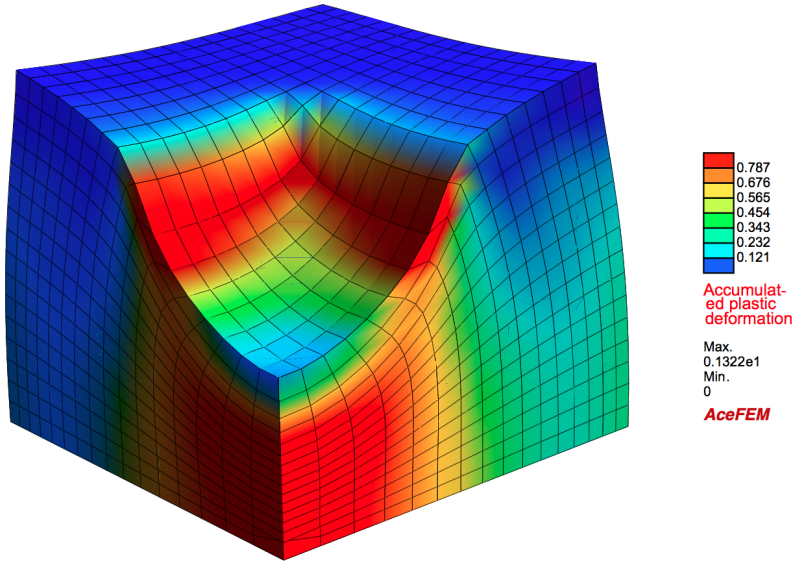

(b) FS-ISO-FEM: isotropic hardening

Figure 6.4: Accumulated plastic deformation and final deformed mesh for p =450 MPa.

6.2 Cylindrical Thick Shell

The next example is the three-dimensional thick cylindrical shell. So, we consider a geometry which cannot be represented exactly by piecewise linear polynomials. It was studied in Reference [113] as a benchmark for the finite strain isotropic hardening model.

The geometry and boundary conditions are represented in figure 6.5. The reference line pressure was set up as 1 kN/mm and the deflection of point A was measured. In its turn, the mechanical properties are described in Table 6.3, where the hardening law was considered linear. Both IGA and FEM isotropic hardening finite strain formulations are compared with the HEXA8-E3 and 6-P SHELL formulations, developed in [113].

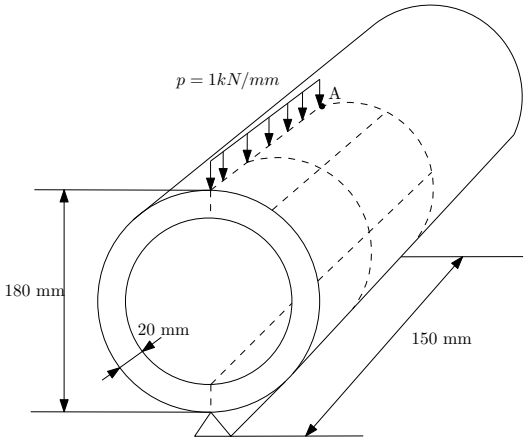

Figure 6.5: Cylindrical shell geometry and boundary conditions.

Table 6.3: Cylindrical shell mechanical properties.

Young Modulus	E =200000 MPa
Poisson's ratio	v =0.2
Yield Stress	s_Y=200 MPa
Isotropic Hardening Modulus	K =2500 MPa

Regarding the geometry, for symmetry reasons only a quarter of the cylinder was considered. Now, if we focus our attention to Figure 6.6, only second order NURBS functions are capable to represent exactly the geometry in IGA model for this case. The Figure 6.6 contains an isogeometric mesh with 4 knot spans and a finite element mesh with the same number of elements. The geometrical differences between the two discretizations are quite evident in this example. At one side the geometry is exact irrespective the mesh refinement and, on the other side, adding more elements to the model we only can get an approximate geometry.

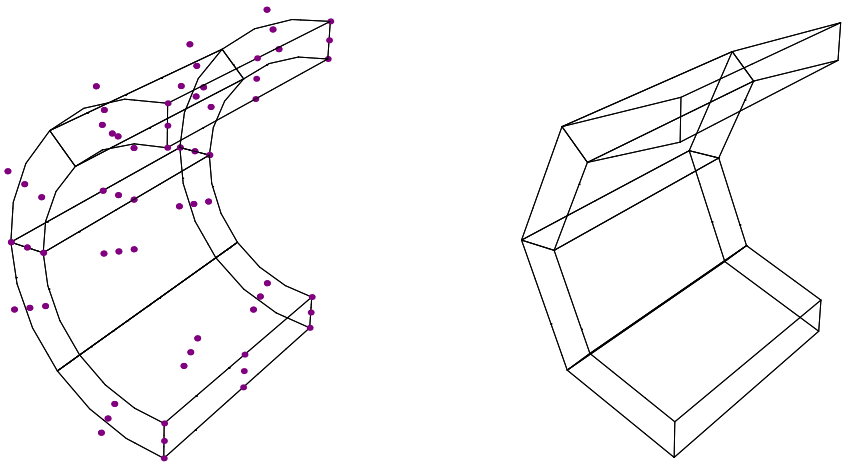

(a) Isogeometric mesh (b) Finite element mesh

Figure 6.6: Differences between Isogeometric and finite element meshes for cylindrical shell geometry.

The Figure 6.7 shows the point A deflection as a function of the load factor. Both FEM and IGA formulations are between the expected values, according to the reference [].

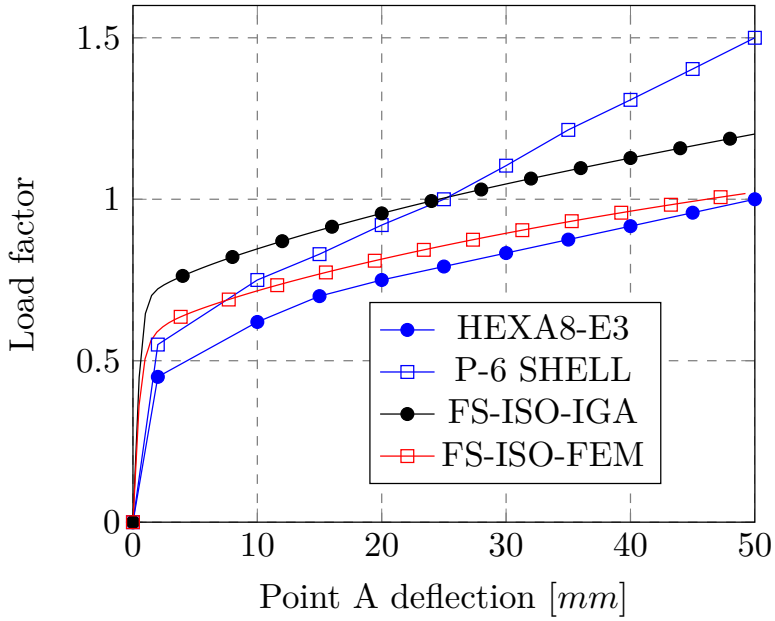

Figure 6.7: Comparisson of Point A deflection for different values of load factor.

To conclude this example we show the accumulated plastic strain field in Figure 6.8 after the 50 mm vertical displacement. Note that the finite element mesh is highly refined using linear interpolation function whereas the isogeometric mesh is coarse with second degree NURBS functions.

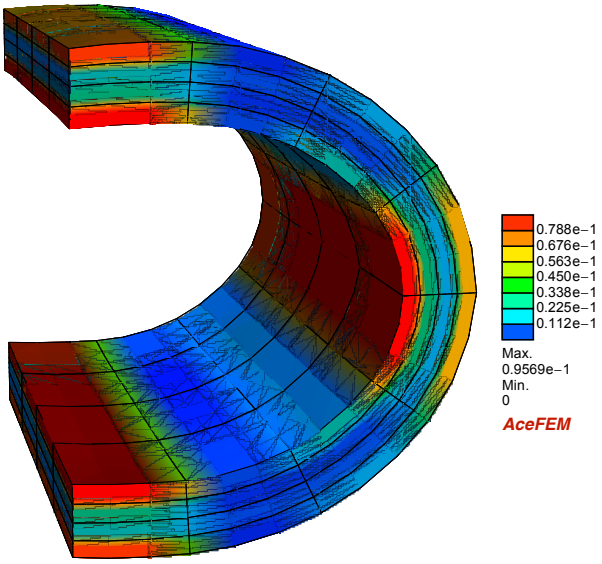

(a) Isogeometric mesh

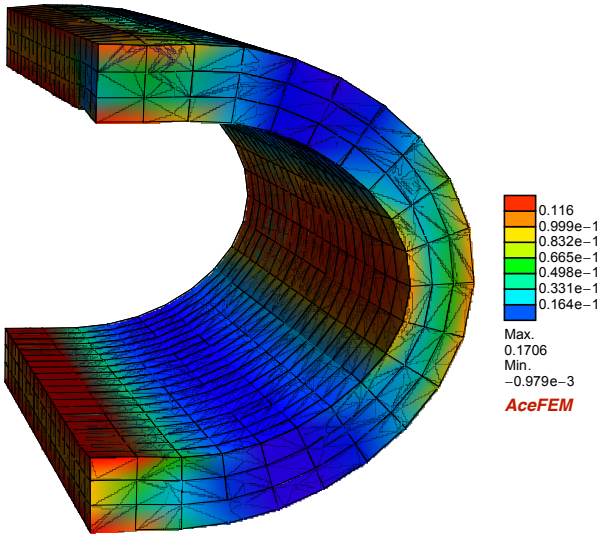

(b) Finite element mesh

Figure 6.8: Accumulated plastic deformation and final deformed mesh for cylindrical shell.

6.3 Clamped Bar

In the third example, we analyse the IGA kinematic hardening model by comparison with the FE formulation. The clamped bar presented in Figure 6.9 is subjected to 5 cycles following the pattern according to the Figure 6.10 where top mesh nodes vertical displacement varies between $\pm$ 0.25 mm.

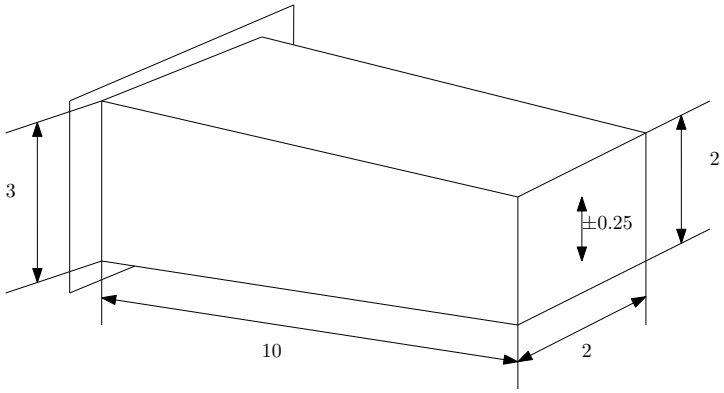

Figure 6.9: Clamped bar geometry and boundary conditions.

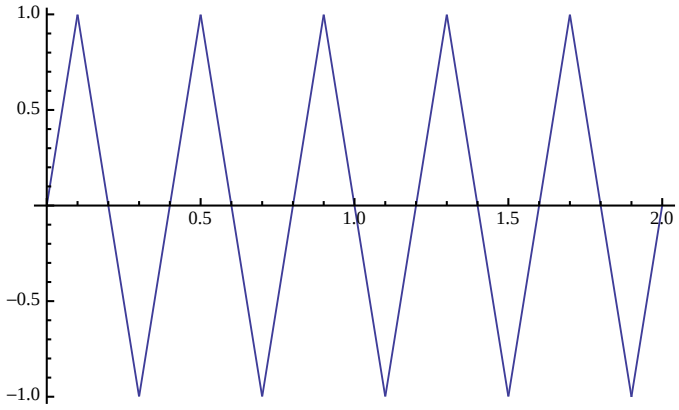

Figure 6.10: Load path of clamped bar.

The bar was obligated to travel between ± 0.25 mm and have the mechanical properties of the X52 alloy steel. The elastic and isotropic hardening mechanical properties were obtained in IDMEC/INEGI-FEUP facilities with tensile experimental test and are exposed in Table 6.4. The kinematic related ones where arbitrated with the most common values for alloy steels.

Table 6.4: Cylindrical shell mechanical properties.

Young Modulus	E =206900MPa
Poisson's Ratio	v =0.29
Yield Stress	τ_Y=449.99 MPa
Isotropic Hardening Modulus	K =129.24 MPa
Limite isotropic Hardening	R_{inf}=265.00 MPa
Saturation Exponent	δ=16.93
Kinematic Hardening Modulus	H_k=1000 MPa
Kinematic saturation	b_{sat}=0.001

However, in order to test the kinematic model we need to know the differences of the structure response with the situation where there is no kinematic hardening. The results from Figure 6.11a were obtained setting up all hardening parameters to zero and the Figure 6.11b presents the results only with kinematic hardening. For this cases, the structure behaviour is practically the same for both IGA and FEM models. On the other hand, Figure 6.11c shows the structure response with only isotropic hardening and Figure 6.11d with both types of hardening.

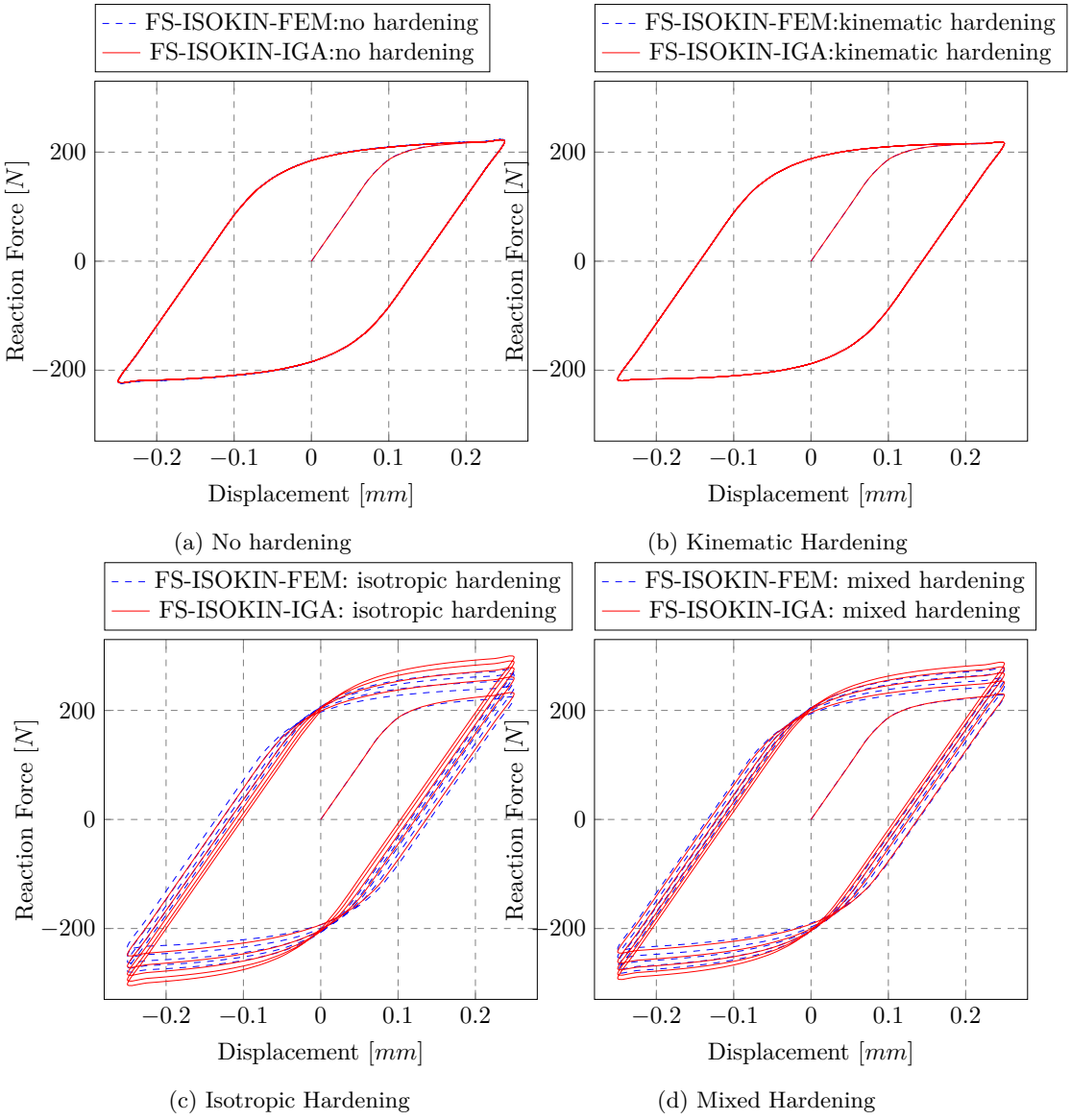

(a) No hardening

(b) Kinematic Hardening

(c) Isotropic Hardening

(d) Mixed Hardening

Figure 6.11: Reaction force along the 5 cycles considering the different hardening situations.

For the last two cases the IGA model get a stiffer behaviour again. However, in order to evaluate the kinematic and isotropic hardening effects, the Figure 6.12 shows the difference

relative to the first cycle, in percentage, of the absolute value of the difference between peak reaction forces of each cycle.

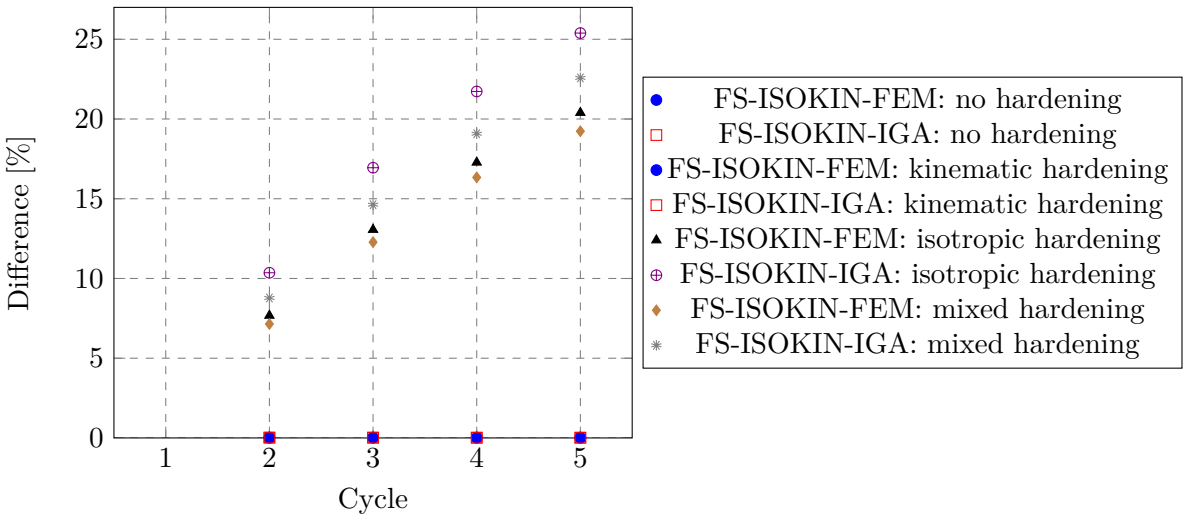

Figure 6.12: Difference between peak forces for each cycle with respect to the first cycle.

In the case of isotropic hardening only, the tensile yield strength is increased at each cycle and, at the same time, the compressive stress also get increased (absolute value). This corresponds to a situation where the radius of the yield surface is increased with no shape modifications The difference between the yield strength get increased in each cycle. However in the case of kinematic hardening we observed Bauschinger's effect. It means the tensile yield strength is increased and the compressive strength get reduced, but the difference remains always constant. The shape and size of the yield surface remains constant.

This behaviour is confirmed by results presents in Figure 6.12 and Table 6.5. The difference gets higher along the cycles for both isotropic and mixed models. However the increase on mixed model is less than the isotropic model because the compression yield strength trends to be the same as the tensile yield strength at each cycle.

Table 6.5: Difference between peak reaction forces of each cycle with respect to the first cycle for IGA mixed hardening model. Values in Newtons [N].

Cycle	No hardening	Kinematic	Isotropic	Mixed
2	0.082	0.090	49.547	41.311
3	0.082	0.087	81.048	68.845
4	0.077	0.079	103.922	89.782
5	0.072	0.072	121.427	106.2706

In order to emphasise the differences between the two kinds of hardening, the clamped bar is subjected again to 5 cycles following the pattern according to the Figure 6.13.

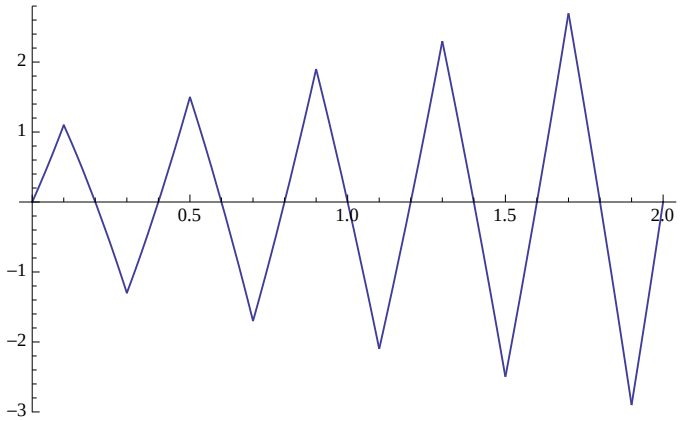

Figure 6.13: Second load path of the clamped bar.

In this situation the magnitude of the displacements is increased at each cycle and the results are presented in Figure 6.14.

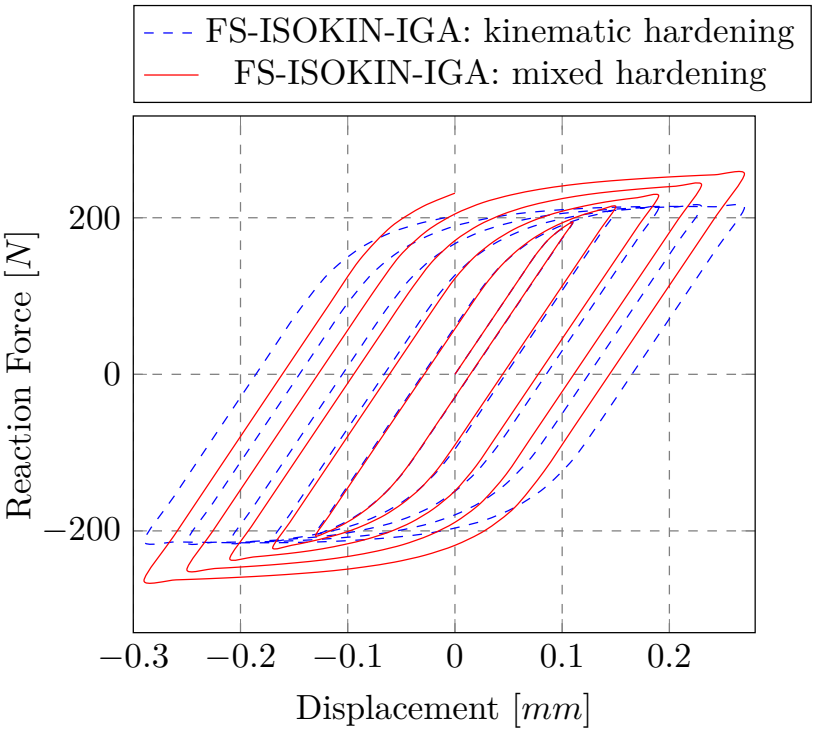

Figure 6.14: Reaction force of the clamped bar along the 5 cycles and following the second pattern.

6.4 Plane stress specimen

The last example focus on a tensile test including all the models developed so far and introduces the Lemaitre damage-based model. The specimen have the same properties of the clamped bar (Table 6.4) and the geometry is showed in Figure 6.15. For symmetry

reasons only half of the specimen was meshed. A displacement of 0.15 mm is applied in the top mesh.

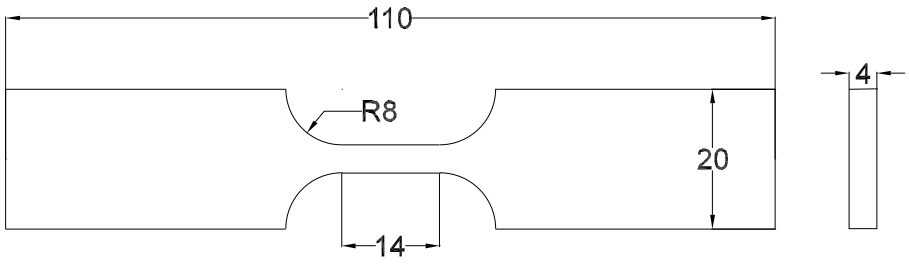

Figure 6.15: Main dimensions of the specimen [mm].

For this case, the specimen was divided into 3 individual meshes, as show in Figure 6.16: the reduced, transition, and the top mesh.

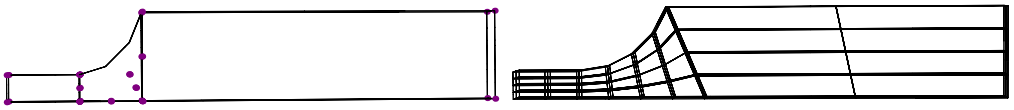

(a) IGA specimen (b) FEM specimen

Figure 6.16: Comparisson between IGA and FEM specimen meshes.

Once again, the IGA mesh requires a second order NURBS in the transition section to describe exactly the geometry and the FEM mesh only gets an approximate shape with the successive refinements[2].

The results of the tensile test are presented in Figure 6.17. The IGA and FEM specimens were composed by 3570 and 3834 DOF, respectively.

[2]The images presented do not show the mesh used for the simulations. They are only coarse meshes to show the differences from both discretisations.

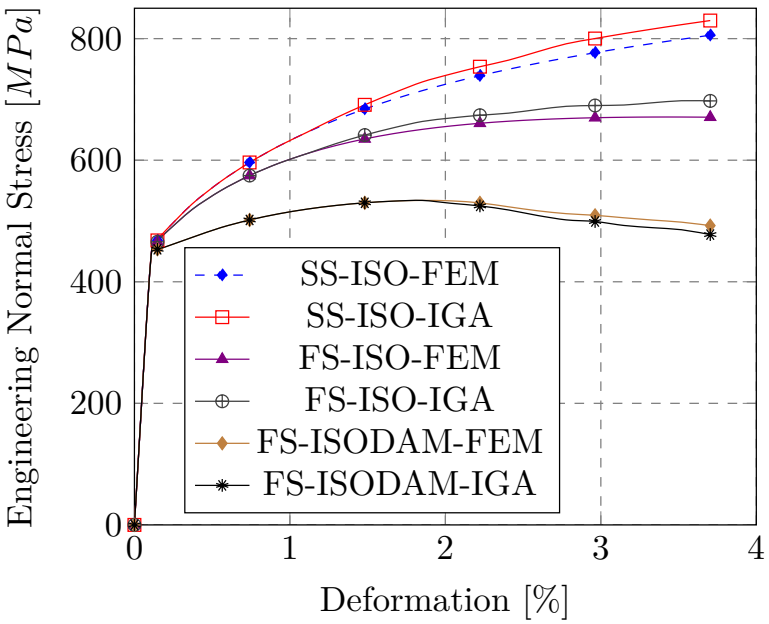

Figure 6.17: Engineering normal stress versus deformation for the tensile test.

Both small and finite strain models without damage have an increase in the yield strength throughout the simulation. In the damaged models, because the specimen suffer an damage increase along the simulation, the softening behaviour starts from a smaller ultimate strength value. The softening slope of the FS-ISODAM-IGA differs from FS-ISODAM-FEM. This may be related to the pathological dependence of the damage variable on the mesh refinement. Further investigations on this subject need to be applied.

6.5 Concluding Remarks

In a general way, the isogeometric elements get a stiffer behaviour by comparison with the finite elements. The use of second order NURBS allowed the exact description of the cylindrical shell and the tensile specimen while the finite element mesh only produced approximated geometries. The small strain model diverges from the finite strain equivalent when the displacements get bigger, as expected.

The kinematic hardening effects were noticed by comparison with the isotropic hardening models.

Concerning the damaged model, the softening regime was verified. However, further studies need to be applied in order to establish the isogeometric mesh influence in the final solution.

Chapter 7

Conclusions and Future Work

7.1 Conclusions

In this work, the isogeometric discretisation was applied to the study of non-linear models.

First, the isogeometric elements were applied to small strain models with isotropic hardening. This model has material non-linearity behaviour whereas the final geometric configuration can be considered linear. When the IGA element was applied into the finite strain model with isotropic hardening, a second type of non-linearity appeared. The discrepancy between these two models is evident when the magnitude of the natural boundary conditions is increased, as expected. Regarding the comparison with the FEM model, the results are identical but the IGA elements got a stiffer response. Also, the higher order NURBS solutions with coarse meshes appeared with a good approximation.

In the second phase of the work, the isogeometric element was introduced into a mixed hardening model. The Baushinger's effect is verified and the solution is very close to the FEM model.

Concerning the Lemaitre damage-based models, both models response practically in the same manner in the tensile test. However the slope in the softening regime of the isogeometric model is bigger (in value) than the finite element model. This may be related to the mesh influence on the damage variable but further studies need to be applied.

In general, the elastoplastic results shows that the IGA discretisation process were successfully implemented. However, further corrections related to the F-bar method need to be applied. The exaggerated stiffer response of isogeometric models is probably due to the fact that the F-bar method was implemented over knot spans rather than over the patch. The major benefit on using isogeometric elements were the exact description of the geometry. However, its main disadvantage, when compared to the FEM, is a higher computational cost.

Additionally, the managing of these, more or less, complex models was possible due to symbolic and algebraic capabilities of the AceGen systems. It allows a knowledge of the formulations based on its physical meaning rater than the numerical methods to solve the derivatives. The establishment of the constitutive equations at the element level is performed to evaluate the elementary residual vector and elementary consistent tangential matrix. All others steps are intrinsic. This brings the advantage to create new and upgraded formulations in a easy way, however we take the risk of not understanding all the steps and substeps that are included in a traditional FE numerical interface. Furthermore, the AceGen systems were very useful to create prototype models and to confirm the convergence of the isogeometric approach in some variety of problems. However, the implementation into traditional numerical codes is essential to get stability and reach fully developed isogeometric models.

7.2 Future Work

For future works it will be important to address more examples using the Lemaitre damage-based model in order to evaluate the mesh dependence of the formulation.

The application of an sensibility analysis for all developed models is also relevant. It will allows to know if the models are stable by the variation of a certain parameters such the material properties and the geometry of the model.

Another relevant aspect it will be the implementation of the Tangent and Residual created routines into commercial softwares such as Abaqus or Ansys in order to evaluate the models using complex geometries.

Finally, the experimental validation trough tensile and fatigue tests will help in the validation of the models.

Appendix A

Non-Local Damage

A.1 Non-Local Damage Variable

Usually, the CDM models are rooted in a local manner. That is, the material behavior is represented by a point-wise constitutive law. However, this assumption causes a pathological mesh dependency when the structure is under a softening regime.

The non-local approaches incorporates an intrinsic length into the traditional CDM theory and, if properly formulated, overcomes the mesh dependence problem. There are two types of non-local theories: gradient-enhanced or integral-type formulations.

The use of gradient-dependent constitutive models in ductile material have been extensively developed [114–118] but only a limited number of integral-type works have been devoted to model ductile materials [119].

While a diffuse equation and an additional degree of freedom are added to the structural problem in gradient-enhanced approaches, the integral-type formulations do not require this extras. On the other hand, the integral-type formulation needs to ensure the loading-unloading conditions on the material level [8].

In this section we pretend to provide a suitable integral-type non-local theory for finite strain models proposed by [8]. This formulation is based on a thermodynamical non-local framework [120] and adopts a well stablished multiplicative hyperelasto-plastic decomposition of the deformation gradient [121, 122].

Failure in ductile metals is closely related to the localisation of damage. Therefore, damage is regarded as the optimal choice of variable to be enhanced by non-locality, that is, the damage variable of a certain point is averaged within a finite volume V , with radius l_r , as illustrated in figure A.1.

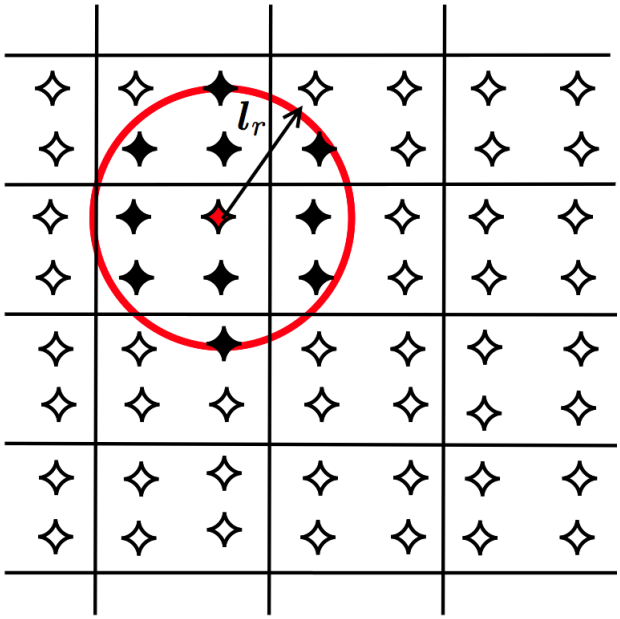

Figure A.1: Definition of the non-local averaging volume [2].

The radius l_r is often termed regularisation or characteristic length, as it acts as a localisation limiter. Then, non-local damage, $\bar{D}(\boldsymbol{x})$, may be defined in function of local damage D by means of the spatially weighted averaging integral as follows:

$$\bar{D}(\boldsymbol{x}) = \int_V \beta(\boldsymbol{x},\boldsymbol{\xi})\, D(\boldsymbol{\xi})\, dV(\boldsymbol{\xi}) \tag{A.1}$$

where $\beta(\boldsymbol{x},\boldsymbol{\xi})$ is an averaging operator defined as [7, 123]:

$$\beta(\boldsymbol{x},\boldsymbol{\xi}) = \frac{\alpha(\boldsymbol{x},\boldsymbol{\xi})}{\Omega(\boldsymbol{x})} \tag{A.2}$$

in which, $\alpha(\boldsymbol{x},\boldsymbol{\xi})$ is the following weighting function

$$\alpha(\boldsymbol{x},\boldsymbol{\xi}) = \left\langle 1 - \frac{\|x-\xi\|^2}{{l_r}^2} \right\rangle^2 \tag{A.3}$$

and Ω is usually designated as representative volume [124] that may be defined as

$$\Omega(\boldsymbol{x}) = \int_V \alpha(\boldsymbol{x},\boldsymbol{\xi})\, dV(\boldsymbol{\xi}) \tag{A.4}$$

In these equations, $\bar{D}(\boldsymbol{x})$ represents the damage measurement at a material generic point denoted by $\boldsymbol{x}$, which has been averaged over the defined finite volume V, containing the set of points ε. The size of the non-local volume is dictated by the constitutive parameter l_r which takes the influence of the microstructure in a averaging sense. This

quantity cannot be measured directly from experiments but rather obtained through inverse analysis based on experimental evidence [7]. Note also that the weighting function $\alpha(\boldsymbol{x},\boldsymbol{\xi})$ reach a maximum at the origin and decreases as the distance of neighboring points increase.

Furthermore, the averaging operator $\beta(\boldsymbol{x},\boldsymbol{\xi})$ is assumed to be independent of the deformation history and is evaluated at the undeformed configuration. Therefore, the damage evolution $\dot{\bar{D}}(\boldsymbol{x})$ can be readily determined:

$$\dot{\bar{D}}(\boldsymbol{x}) = \int_V \beta(\boldsymbol{x},\boldsymbol{\xi})\dot{\gamma}\frac{1}{1-D(\boldsymbol{\xi})}\left(\frac{-Y}{r}\right)^s dV(\boldsymbol{\xi}) \tag{A.5}$$

As the effects of damage and plasticity are considered in a decoupled way, the regularization of the damage variable D does not affect the plasticity-related variables. The local constitutive model presented in this section can be directly extended to the non-local case, replacing the local damage variable by its non-local counterpart. The detailed thermodynamical derivation of the non-local integral constitutive model may be found in [120].

References

[1] SINTEF, "Sintef-terrific (website:http://www.sintef.no/projectweb/isogeometric-analysis/): Isogeometric analysys," Nov. 2009.

[2] M. Seabra and J. de Sá, "Continuous-Discontinuous Model for Ductile Fracture," *NUMIFORM 2010: Proceedings of the 10th International Conference on Numerical Methods in Industrial Forming Processes, dedicated to Professor O.C. Zienkiewicz (1921-2009) : Pohang, Republic of Korea, 13-17 June 2010*, 2010.

[3] G. Dhondt, *The finite element method for three-dimensional thermomechanical applications*. Hoboken, NJ: Wiley, 2004.

[4] F. M. Andrade Pires, J. M. A. César de Sá, L. Costa Sousa, and R. M. Natal Jorge, "Numerical modelling of ductile plastic damage in bulk metal forming," *International Journal of Mechanical Sciences*, vol. 45, pp. 273–294, Feb. 2003.

[5] E. A. de Souza Neto, D. Perić, and D. R. J. Owen, "A model for elastoplastic damage at finite strains: algorithmic issues and applications," *Engineering Computations*, vol. 11, pp. 257–281, Dec. 1994.

[6] J. Lemaitre, *A course on damage mechanics*. Springer Verlag, 1996.

[7] Z. P. Bazant and M. Jirásek, "Nonlocal integral formulations of plasticity and damage: survey of progress," *Journal of Engineering Mechanics*, 2002.

[8] F. X. C. Andrade, *Non-local Modelling of Ductile Damage: Formulation and Numerical Issues* . PhD thesis, FEUP, May 2000.

[9] J. Lemaitre and R. Desmorat, *Engineering Damage Mechanics*. Ductile, Creep, Fatigue and Brittle Failures, Springer, Jan. 2006.

[10] S. Oller and E. Chaves, "Fractura mecánica: un enfoque global," 2000.

[11] P. G. Forrest, *Fatigue of metals*. Pergamon, 1962.

[12] S. S. Manson and G. R. Halford, "Re-examination of cumulative fatigue damage analysis—an engineering perspective," *Engineering Fracture Mechanics*, vol. 25, pp. 539–571, Jan. 1986.

[13] L. F. Coffin, Jr., "The Stability of Metals Under Cyclic Plastic Strain," *Journal of Fluids Engineering*, vol. 82, sep 1960.

[14] J.-L. Chaboche, "Continuous damage mechanics — A tool to describe phenomena before crack initiation," *Nuclear Engineering and Design*, vol. 64, pp. 233–247, Apr. 1981.

[15] J. L. Chaboche, "Constitutive equations for cyclic plasticity and cyclic viscoplasticity," *International Journal of Plasticity*, vol. 5, pp. 247–302, Jan. 1989.

[16] J. Chaboche, "Time-independent constitutive theories for cyclic plasticity," *International Journal of Plasticity*, vol. 2, no. 2, pp. 149 – 188, 1986.

[17] M. Wallin, M. Ristinmaa, and N. S. Ottosen, "Kinematic hardening in large strain plasticity," *European Journal of Mechanics - A/Solids*, vol. 22, pp. 341–356, May 2003.

[18] E. A. de Souza Neto, D. Peric, and D. R. J. Owen, *Computational Methods for Plasticity*. Theory and Applications, John Wiley & Sons, Sept. 2011.

[19] L. M. Kachanov, "Time of the rupture process under creep conditions," *Izv. Akad. Nauk. S.S.R. Otd. Tech. Nauk.*, vol. 8, pp. 26–31, 1958.

[20] J. Lemaitre, "Coupled elasto-plasticity and damage constitutive equations," *Computer Methods in Applied Mechanics and Engineering*, vol. 51, pp. 31–49, Sept. 1985.

[21] V. Tvergaard and A. Needleman, "Analysis of the Cup-Cone Fracture in a Round Tensile Bar," *Acta Metallurgica*, vol. 32, no. 1, pp. 157–169, 1984.

[22] T. Hughes, J. Cottrell, and Y. Bazilevs, "Isogeometric analysis: Cad, finite elements, nurbs, exact geometry and mesh refinement," *Computer Methods in Applied Mechanics and Engineering*, vol. 194, no. 39 – 41, pp. 4135 – 4195, 2005.

[23] J. Cottrell, A. Reali, Y. Bazilevs, and T. Hughes, "Isogeometric analysis of structural vibrations," *Computer Methods in Applied Mechanics and Engineering*, vol. 195, no. 41– 43, pp. 5257 – 5296, 2006. John H. Argyris Memorial Issue. Part II.

[24] T. Dokken, E. Quak, and V. Skytt, "Requirements from Isogeometric Analysis for changes in product design ontologies," in *Proceedings of the FOCUS K3D conference ...*, 2010.

[25] W. G. Strang and G. J. Fix, *Analysis of the Finite Elements Method (Prentice-Hall Series in Automatic Computation)*. Prentice Hall, 1973.

[26] J. Cottrell, T. Hughes, and A. Reali, "Studies of refinement and continuity in isogeometric structural analysis," *Computer Methods in Applied Mechanics and Engineering*, vol. 196, no. 41– 44, pp. 4160 – 4183, 2007.

[27] J. Cottrell, *Isogeometric analysis toward integration of CAD and FEA*. Chichester, West Sussex, U.K. Hoboken, NJ: Wiley, 2009.

[28] J. Cottrell, T. Hughes, and A. Reali, "Studies of refinement and continuity in isogeometric structural analysis," *Computer Methods in Applied Mechanics and Engineering*, vol. 196, no. 41–44, pp. 4160 – 4183, 2007.

[29] V. Phu Nguyen, S. P. A. Bordas, and T. Rabczuk, "Isogeometric analysis: an overview and computer implementation aspects," *ArXiv e-prints*, May 2012.

[30] W. A. Wall, M. A. Frenzel, and C. Cyron, "Isogeometric structural shape optimization," *Computer Methods in Applied Mechanics and Engineering*, vol. 197, no. 33–40, pp. 2976 – 2988, 2008.

[31] N. D. Manh, A. Evgrafov, A. R. Gersborg, and J. Gravesen, "Isogeometric shape optimization of vibrating membranes," *Computer Methods in Applied Mechanics and Engineering*, vol. 200, no. 13–16, pp. 1343 – 1353, 2011.

[32] X. Qian and O. Sigmund, "Isogeometric shape optimization of photonic crystals via coons patches," *Computer Methods in Applied Mechanics and Engineering*, vol. 200, no. 25–28, pp. 2237 – 2255, 2011.

[33] X. Qian, "Full analytical sensitivities in nurbs based isogeometric shape optimization," in *Computer Methods in Applied Mechanics and Engineering*, 2010.

[34] R. Simpson, S. Bordas, J. Trevelyan, and T. Rabczuk, "A two-dimensional isogeometric boundary element method for elastostatic analysis," *Computer Methods in Applied Mechanics and Engineering*, vol. 209–212, no. 0, pp. 87 – 100, 2012.

[35] M. Scott, R. Simpson, J. Evans, S. Lipton, S. Bordas, T. Hughes, and T. Sederberg, "Isogeometric boundary element analysis using unstructured t-splines," *Computer Methods in Applied Mechanics and Engineering*, vol. 254, no. 0, pp. 197 – 221, 2013.

[36] Y. Bazilevs, V. Calo, J. Cottrell, J. Evans, T. Hughes, S. Lipton, M. Scott, and T. Sederberg, "Isogeometric analysis using t-splines," *Computer Methods in Applied Mechanics and Engineering*, vol. 199, no. 5–8, pp. 229 – 263, 2010. Computational Geometry and Analysis.

[37] T. W. Sederberg, J. Zheng, A. Bakenov, and A. Nasri, "T-splines and t-nurccs," *ACM Trans. Graph.*, vol. 22, pp. 477–484, July 2003.

[38] M. A. Scott, M. J. Borden, C. V. Verhoosel, T. W. Sederberg, and T. J. R. Hughes, "Isogeometric finite element data structures based on bézier extraction of t-splines," *International Journal for Numerical Methods in Engineering*, vol. 88, no. 2, pp. 126–156, 2011.

[39] D. Burkhart, B. Hamann, and G. Umlauf, "Iso-geometric finite element analysis based on catmull-clark : ubdivision solids," *Computer Graphics Forum*, vol. 29, no. 5, pp. 1575–1584, 2010.

[40] A. Wawrzinek, K. Hildebrandt, and K. Polthier, "Koiter's thin shells on catmull-clark limit surfaces.," in *VMV* (P. Eisert, J. Hornegger, and K. Polthier, eds.), pp. 113–120, Eurographics Association, 2011.

[41] R. Sevilla, S. Fernández-Méndez, and A. Huerta, "3d nurbs-enhanced finite element method (nefem)," *International Journal for Numerical Methods in Engineering*, vol. 88, no. 2, pp. 103–125, 2011.

[42] R. Sevilla, S. Fernández-Méndez, and A. Huerta, "Nurbs-enhanced finite element method (nefem)," *Archives of Computational Methods in Engineering*, vol. 18, no. 4, pp. 441–484, 2011.

[43] C. V. Verhoosel, M. A. Scott, R. de Borst, and T. J. R. Hughes, "An isogeometric approach to cohesive zone modeling," *International Journal for Numerical Methods in Engineering*, vol. 87, no. 1-5, pp. 336–360, 2011.

[44] R. Schmidt, R. Wüchner, and K.-U. Bletzinger, "Isogeometric analysis of trimmed nurbs geometries," *Computer Methods in Applied Mechanics and Engineering*, vol. 241–244, no. 0, pp. 93 – 111, 2012.

[45] H.-J. Kim, Y.-D. Seo, and S.-K. Youn, "Isogeometric analysis with trimming technique for problems of arbitrary complex topology," *Computer Methods in Applied Mechanics and Engineering*, vol. 199, no. 45–48, pp. 2796 – 2812, 2010.

[46] S. K. Kleiss, B. Jüttler, and W. Zulehner, "Enhancing isogeometric analysis by a finite element-based local refinement strategy," *Computer Methods in Applied Mechanics and Engineering*, vol. 213–216, no. 0, pp. 168 – 182, 2012.

[47] H. Speleers, C. Manni, F. Pelosi, and M. L. Sampoli, "Isogeometric analysis with powell–sabin splines for advection–diffusion–reaction problems," *Computer Methods in Applied Mechanics and Engineering*, vol. 221–222, no. 0, pp. 132 – 148, 2012.

[48] P. Bornemann and F. Cirak, "A subdivision-based implementation of the hierarchical b-spline finite element method," *Computer Methods in Applied Mechanics and Engineering*, vol. 253, no. 0, pp. 584 – 598, 2013.

[49] A.-V. Vuong, C. Giannelli, B. Jüttler, and B. Simeon, "A hierarchical approach to adaptive local refinement in isogeometric analysis," *Computer Methods in Applied Mechanics and Engineering*, vol. 200, no. 49–52, pp. 3554 – 3567, 2011.

[50] D. Schillinger, L. Dedè, M. A. Scott, J. A. Evans, M. J. Borden, E. Rank, and T. J. Hughes, "An isogeometric design-through-analysis methodology based on adaptive hierarchical refinement of nurbs, immersed boundary methods, and t-spline cad surfaces," *Computer Methods in Applied Mechanics and Engineering*, vol. 249–252, no. 0, pp. 116 – 150, 2012. Higher Order Finite Element and Isogeometric Methods.

[51] N. Nguyen-Thanh, J. Kiendl, H. Nguyen-Xuan, R. Wüchner, K. Bletzinger, Y. Bazilevs, and T. Rabczuk, "Rotation free isogeometric thin shell analysis using pht-splines," *Computer Methods in Applied Mechanics and Engineering*, vol. 200, no. 47–48, pp. 3410 – 3424, 2011.

[52] N. Nguyen-Thanh, H. Nguyen-Xuan, S. Bordas, and T. Rabczuk, "Isogeometric analysis using polynomial splines over hierarchical t-meshes for two-dimensional elastic solids," *Computer Methods in Applied Mechanics and Engineering*, vol. 200, no. 21–22, pp. 1892 – 1908, 2011.

[53] T. Dokken, T. Lyche, and K. F. Pettersen, "Polynomial splines over locally refined box-partitions," *Computer Aided Geometric Design*, vol. 30, no. 3, pp. 331 – 356, 2013.

[54] H. Wang, Y. He, X. Li, X. Gu, and H. Qin, "Polycube splines," *Computer-Aided Design*, vol. 40, no. 6, pp. 721 – 733, 2008. Selected Papers from the ACM Solid and Physical Modeling Symposium 2007 ACM Symposium on Solid and Physical Modeling and Applications.

[55] M. R. Dörfel, B. Jüttler, and B. Simeon, "Adaptive isogeometric analysis by local h-refinement with t-splines," *Computer Methods in Applied Mechanics and Engineering*, vol. 199, no. 5–8, pp. 264 – 275, 2010. Computational Geometry and Analysis.

[56] M. Scott, X. Li, T. Sederberg, and T. Hughes, "Local refinement of analysis-suitable t-splines," *Computer Methods in Applied Mechanics and Engineering*, vol. 213–216, no. 0, pp. 206 – 222, 2012.

[57] A. Buffa, D. Cho, and G. Sangalli, "Linear independence of the t-spline blending functions associated with some particular t-meshes," *Computer Methods in Applied Mechanics and Engineering*, vol. 199, no. 23–24, pp. 1437 – 1445, 2010.

[58] Temizer, P. Wriggers, and T. Hughes, "Contact treatment in isogeometric analysis with nurbs," *Computer Methods in Applied Mechanics and Engineering*, vol. 200, no. 9–12, pp. 1100 – 1112, 2011.

[59] J. Lu, "Isogeometric contact analysis: Geometric basis and formulation for frictionless contact," *Computer Methods in Applied Mechanics and Engineering*, vol. 200, no. 5–8, pp. 726 – 741, 2011.

[60] L. Lorenzis, P. Wriggers, and G. Zavarise, "A mortar formulation for 3d large deformation contact using nurbs-based isogeometric analysis and the augmented lagrangian method," *Computational Mechanics*, vol. 49, no. 1, pp. 1–20, 2012.

[61] L. De Lorenzis, Temizer, P. Wriggers, and G. Zavarise, "A large deformation frictional contact formulation using nurbs-based isogeometric analysis," *International Journal for Numerical Methods in Engineering*, vol. 87, no. 13, pp. 1278–1300, 2011.

[62] M. Matzen, T. Cichosz, and M. Bischoff, "A point to segment contact formulation for isogeometric, nurbs based finite elements," *Computer Methods in Applied Mechanics and Engineering*, vol. 255, no. 0, pp. 27 – 39, 2013.

[63] J. Kiendl, K.-U. Bletzinger, J. Linhard, and R. Wüchner, "Isogeometric shell analysis with kirchhoff–love elements," *Computer Methods in Applied Mechanics and Engineering*, vol. 198, no. 49–52, pp. 3902 – 3914, 2009.

[64] L. B. da Veiga, A. Buffa, C. Lovadina, M. Martinelli, and G. Sangalli, "An isogeometric method for the reissner–mindlin plate bending problem," *Computer Methods in Applied Mechanics and Engineering*, vol. 209–212, no. 0, pp. 45 – 53, 2012.

[65] T.-K. Uhm and S.-K. Youn, "T-spline finite element method for the analysis of shell structures," *International Journal for Numerical Methods in Engineering*, vol. 80, no. 4, pp. 507–536, 2009.

[66] R. Echter, B. Oesterle, and M. Bischoff, "A hierarchic family of isogeometric shell finite elements," *Computer Methods in Applied Mechanics and Engineering*, vol. 254, no. 0, pp. 170 – 180, 2013.

[67] D. Benson, S. Hartmann, Y. Bazilevs, M.-C. Hsu, and T. Hughes, "Blended isogeometric shells," *Computer Methods in Applied Mechanics and Engineering*, vol. 255, no. 0, pp. 133 – 146, 2013.

[68] J. Kiendl, Y. Bazilevs, M.-C. Hsu, R. Wüchner, and K.-U. Bletzinger, "The bending strip method for isogeometric analysis of kirchhoff–love shell structures comprised of multiple patches," *Computer Methods in Applied Mechanics and Engineering*, vol. 199, no. 37–40, pp. 2403 – 2416, 2010.

[69] C. H. Thai, A. Ferreira, E. Carrera, and H. Nguyen-Xuan, "Isogeometric analysis of laminated composite and sandwich plates using a layerwise deformation theory," *Composite Structures*, vol. 104, no. 0, pp. 196 – 214, 2013.

[70] J. Lu, "Circular element: Isogeometric elements of smooth boundary," *Computer Methods in Applied Mechanics and Engineering*, vol. 198, no. 30–32, pp. 2391 – 2402, 2009.

[71] J. Lu and X. Zhou, "Cylindrical element: Isogeometric model of continuum rod," *Computer Methods in Applied Mechanics and Engineering*, vol. 200, no. 1–4, pp. 233 – 241, 2011.

[72] Y. Bazilevs, V. Calo, T. Hughes, and Y. Zhang, "Isogeometric fluid-structure interaction: theory, algorithms, and computations," *Computational Mechanics*, vol. 43, no. 1, pp. 3–37, 2008.

[73] H. Gomez, T. J. Hughes, X. Nogueira, and V. M. Calo, "Isogeometric analysis of the isothermal navier–stokes–korteweg equations," *Computer Methods in Applied Mechanics and Engineering*, vol. 199, no. 25–28, pp. 1828 – 1840, 2010.

[74] P. N. Nielsen, A. R. Gersborg, J. Gravesen, and N. L. Pedersen, "Discretizations in isogeometric analysis of navier–stokes flow," *Computer Methods in Applied Mechanics and Engineering*, vol. 200, no. 45–46, pp. 3242 – 3253, 2011.

[75] Y. Bazilevs, J. Gohean, T. Hughes, R. Moser, and Y. Zhang, "Patient-specific isogeometric fluid–structure interaction analysis of thoracic aortic blood flow due to implantation of the jarvik 2000 left ventricular assist device," *Computer Methods in Applied Mechanics and Engineering*, vol. 198, no. 45–46, pp. 3534 – 3550, 2009. Models and Methods in Computational Vascular and Cardiovascular Mechanics.

[76] Y. Bazilevs and I. Akkerman, "Large eddy simulation of turbulent taylor–couette flow using isogeometric analysis and the residual-based variational multiscale method," *Journal of Computational Physics*, vol. 229, no. 9, pp. 3402 – 3414, 2010.

[77] C. V. Verhoosel, M. A. Scott, T. J. R. Hughes, and R. de Borst, "An isogeometric analysis approach to gradient damage models," *International Journal for Numerical Methods in Engineering*, vol. 86, no. 1, pp. 115–134, 2011.

[78] P. Fischer, M. Klassen, J. Mergheim, P. Steinmann, and R. Müller, "Isogeometric analysis of 2d gradient elasticity," *Computational Mechanics*, vol. 47, no. 3, pp. 325–334, 2011.

[79] H. Gómez, V. M. Calo, Y. Bazilevs, and T. J. Hughes, "Isogeometric analysis of the cahn–hilliard phase-field model," *Computer Methods in Applied Mechanics and Engineering*, vol. 197, no. 49–50, pp. 4333 – 4352, 2008.

[80] A. Masud and R. Kannan, "B-splines and nurbs based finite element methods for kohn–sham equations," *Computer Methods in Applied Mechanics and Engineering*, vol. 241–244, no. 0, pp. 112 – 127, 2012.

[81] C. H. Thai, H. Nguyen-Xuan, N. Nguyen-Thanh, T.-H. Le, T. Nguyen-Thoi, and T. Rabczuk, "Static, free vibration, and buckling analysis of laminated composite Reissner-Mindlin plates using NURBS-based isogeometric approach.," *Int. J. Numer. Methods Eng.*, vol. 91, no. 6, pp. 571–603, 2012.

[82] J. Cottrell, A. Reali, Y. Bazilevs, and T. Hughes, "Isogeometric analysis of structural vibrations," *Computer Methods in Applied Mechanics and Engineering*, vol. 195, no. 41–43, pp. 5257 – 5296, 2006. John H. Argyris Memorial Issue. Part II.

[83] T. Hughes, A. Reali, and G. Sangalli, "Duality and unified analysis of discrete approximations in structural dynamics and wave propagation: Comparison of p-method finite elements with k-method nurbs," *Computer Methods in Applied Mechanics and Engineering*, vol. 197, no. 49–50, pp. 4104 – 4124, 2008.

[84] D. Wang, W. Liu, and H. Zhang, "Novel higher order mass matrices for isogeometric structural vibration analysis," *Computer Methods in Applied Mechanics and Engineering*, vol. 260, no. 0, pp. 92 – 108, 2013.

[85] E. De Luycker, D. J. Benson, T. Belytschko, Y. Bazilevs, and M. C. Hsu, "X-fem in isogeometric analysis for linear fracture mechanics," *International Journal for Numerical Methods in Engineering*, vol. 87, no. 6, pp. 541–565, 2011.

[86] T. Elguedj, Y. Bazilevs, V. Calo, and T. Hughes, "B-bar and f-bar projection methods for nearly incompressible linear and non-linear elasticity and plasticity using higher-order nurbs elements," *Computer Methods in Applied Mechanics and Engineering*, vol. 197, pp. 2732–2762, 2008.

[87] R. P. R. Cardoso and J. M. A. Cesar de Sa, "The enhanced assumed strain method for the isogeometric analysis of nearly incompressible deformation of solids," *International Journal for Numerical Methods in Engineering*, vol. 92, no. 1, pp. 56–78, 2012.

[88] F. Auricchio, L. B. da Veiga, A. Buffa, C. Lovadina, A. Reali, and G. Sangalli, "A fully "locking-free" isogeometric approach for plane linear elasticity problems: A stream function formulation," *Computer Methods in Applied Mechanics and Engineering*, vol. 197, no. 1–4, pp. 160 – 172, 2007.

[89] R. Echter and M. Bischoff, "Numerical efficiency, locking and unlocking of nurbs finite elements," *Computer Methods in Applied Mechanics and Engineering*, vol. 199, no. 5–8, pp. 374 – 382, 2010. Computational Geometry and Analysis.

[90] S. Lipton, J. Evans, Y. Bazilevs, T. Elguedj, and T. Hughes, "Robustness of isogeometric structural discretizations under severe mesh distortion," *Computer Methods in Applied Mechanics and Engineering*, vol. 199, no. 5–8, pp. 357 – 373, 2010. Computational Geometry and Analysis.

[91] N. Collier, D. Pardo, L. Dalcin, M. Paszynski, and V. Calo, "The cost of continuity: A study of the performance of isogeometric finite elements using direct solvers," *Computer Methods in Applied Mechanics and Engineering*, vol. 213–216, no. 0, pp. 353 – 361, 2012.

[92] F. Auricchio, L. B. a. Da Veiga, T. J. R. Hughes, A. Reali, and G. Sangalli, "Isogeometric collocation methods," *Mathematical Models and Methods in Applied Sciences*, vol. 20, no. 11, pp. 2075+, 2010.

[93] F. Auricchio, L. B. da Veiga, T. Hughes, A. Reali, and G. Sangalli, "Isogeometric collocation for elastostatics and explicit dynamics," *Computer Methods in Applied*

Mechanics and Engineering, vol. 249–252, no. 0, pp. 2 – 14, 2012. Higher Order Finite Element and Isogeometric Methods.

[94] T. Hughes, A. Reali, and G. Sangalli, "Efficient quadrature for nurbs-based isogeometric analysis," *Computer Methods in Applied Mechanics and Engineering*, vol. 199, no. 5–8, pp. 301 – 313, 2010. Computational Geometry and Analysis.

[95] F. Auricchio, F. Calabrò, T. Hughes, A. Reali, and G. Sangalli, "A simple algorithm for obtaining nearly optimal quadrature rules for nurbs-based isogeometric analysis," *Computer Methods in Applied Mechanics and Engineering*, vol. 249–252, no. 0, pp. 15 – 27, 2012. Higher Order Finite Element and Isogeometric Methods.

[96] J. Korelc, "AceGen Manual," pp. 1–270, Jan. 2011.

[97] L. Piegl, *The NURBS book*. Berlin New York: Springer, 1997.

[98] D. F. Rogers, *An Introduction to NURBS: With Historical Perspective*. Morgan Kaufmann, 2000.

[99] T. Elguedj, Y. Bazilevs, and V. M. Calo, "B/F-bar projection methods for nearly incompressible analysis using higher-order NURBS elements," *9th US National ...*, 2007.

[100] K. Krabbenhoft, *Basic Computational Plasticity*. July 2010.

[101] G. A. Holzapfel, "On Large Strain Viscoelasticity: Continuum formulation and finite element applications to elastomeric structures.," *International Journal for Numerical Methods in Engineering*, vol. 39, no. 22, pp. 3903–3926, 1996.

[102] C. Truesdell and R. Baierlein, "Rational Thermodynamics," *American Journal of Physics*, vol. 53, pp. 1020–1021, Oct. 1985.

[103] W. Dettmer and S. Reese, "On the theoretical and numerical modelling of Armstrong–Frederick kinematic hardening in the finite strain regime," *Computer Methods in Applied Mechanics and ...*, 2004.

[104] R. M. N. Jorge, "Teoria da plasticidade." Departamento de Engenharia Mecanica e Gestao Industrial. Faculdade de Engenharia, 2004.

[105] F. Dunne and N. Petrinic, *Introduction to Computational Plasticity*. Oxford University Press, USA, 2005.

[106] M. P. L. Parente, *Análise elasto-plástica de estruturas tipo casca com comportamento anisitrópico*. PhD thesis, Universidade do Porto. Faculdade de Engenharia, 2003.

[107] "Stress computation in elastoplasticity," *Engineering Computations*, vol. 1, pp. 42 – 51, 1985.

[108] S. Commend and T. Zimmermann, "Object-oriented nonlinear finite element programming: a primer," *Advances in Engineering Software*, vol. 32, no. 8, pp. 611 – 628, 2001.

[109] P. Wriggers, *Nonlinear Finite Element Methods*. Berlin, Heidelberg: Springer, nov 2008.

[110] J. Korelc, "AceFEM Manual," 2009.

[111] J. Korelc, "Multi-language and multi-environment generation of nonlinear finite element codes," *Engineering with computers*, 2002.

[112] J. Korelc, "Automation of primal and sensitivity analysis of transient coupled problems," *Computational Mechanics*, vol. 44, no. 5, pp. 631–649, 2009.

[113] D. Roehl and E. Ramm, "Large elasto-plastic finite element analysis of solids and shells with the enhanced assumed strain concept," *International Journal of Solids and Structures*, vol. 33, no. 20–22, pp. 3215 – 3237, 1996.

[114] J. C. de Sá, P. Areias, and C. Zheng, "Damage modelling in metal forming problems using an implicit non-local gradient model," *Computer methods in applied ...*, 2006.

[115] R. Engelen, M. Geers, and F. Baaijens, "Nonlocal implicit gradient-enhanced elastoplasticity for the modelling of softening behaviour," *International Journal of Plasticity*, 2003.

[116] M. Geers and R. Ubachs, "Strongly non-local gradient-enhanced finite strain elastoplasticity," *International Journal for ...*, 2003.

[117] J. Mediavilla, R. Peerlings, and M. Geers, "A nonlocal triaxiality-dependent ductile damage model for finite strain plasticity," *Computer methods in applied ...*, 2006.

[118] S. Ricci and M. Brünig, "Numerical analysis of nonlocal anisotropic continuum damage," *International Journal of Damage Mechanics*, 2007.

[119] V. TVERGAARD and A. NEEDLEMAN, "Effects of Nonlocal Damage in Porous Plastic Solids," *International Journal of Solids and Structures*, vol. 32, no. 8-9, pp. 1063–1077, 1995.

[120] C. Polizzotto, G. Borino, and P. Fuschi, "A thermodynamically consistent formulation of nonlocal and gradient plasticity ," *Mechanics Research Communications*, 1998.

[121] D. Peric, D. Owen, and M. E. Honnor, "A Model for Finite Strain Elastoplasticity Based on Logarithmic Strains - Computational Issues," *Computer Methods in Applied Mechanics and Engineering*, vol. 94, pp. 35–61, Jan. 1992.

[122] J. C. Simo and M. Ortiz, "A unified approach to finite deformation elastoplastic analysis based on the use of hyperelastic constitutive equations," *Computer Methods in Applied Mechanics and Engineering*, vol. 49, pp. 221–245, June 1985.

[123] M. Jirásek, "Nonlocal damage mechanics," *Revue Européenne de Génie Civil*, 2007.

[124] G. Borino, B. Failla, and F. Parrinello, "A symmetric nonlocal damage theory," *International Journal of Solids and Structures*, vol. 40, pp. 3621–3645, June 2003.